SOFC materials characterization

Vladislav A. Sadykov

Boreskov Institute of catalysis, Novosibirsk, Russia

Basic characteristics determining performance of SOFC materials

- 1. Phase composition (XRD)
- 2. Real structure and microstructure (XRD, neutron diffraction, WAXS, TEM and SEM with EDX, EXAFS, FTIRS, Raman, MAS NMR, Mössbauer)
- 3. Texture (porosity, TPB length): Hg porosimetry, Ar adsorption isotherms, X-ray SAS, elemental mapping
- 4. Surface properties (composition, structure): XPS, SIMS
- 5. Transport characteristics (impedance)
- 6. Oxygen mobility, bonding strength and reactivity of surface sites (oxygen isotope exchange, TPD, microcalorimetry, weight and conductivity relaxation)

XRD

- Basic principle: diffraction of X-rays from certain planes of crystallites results in peak situated at some diffraction angle 2θ

- Peak Integral intensity determined by electronic density of planes (metal cations), broadening by crystal sizes in this direction and extended defects (stacking faults, twins, microstrains)

- Standard technique: commercial diffractometers, diffraction from a packed layer of polycrystalline samples, Cu K_α radiation, Scherrer equation etc.

-   Sophisticated XRD technique: synchrotron radiation, much higher precision

Typical XRD diffraction patterns
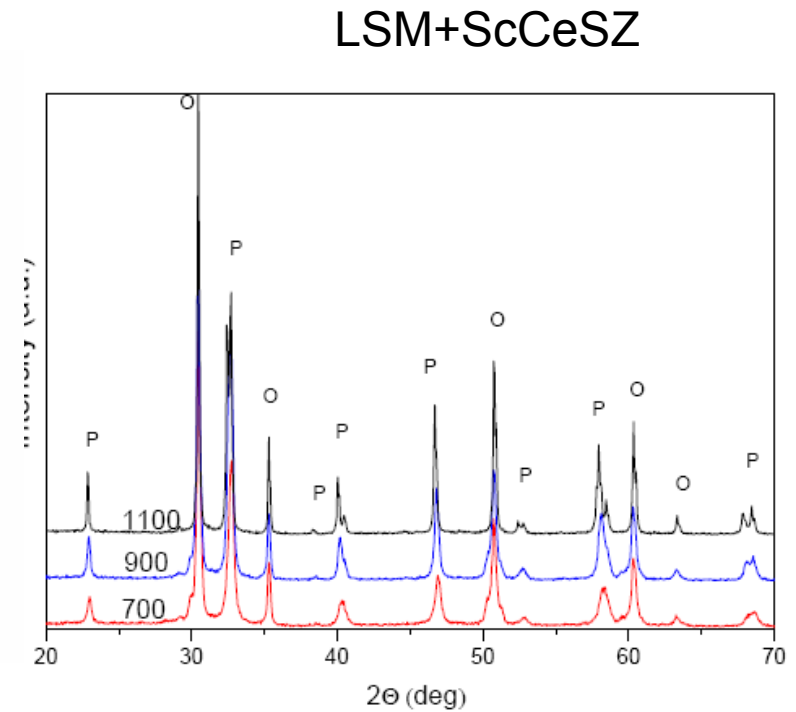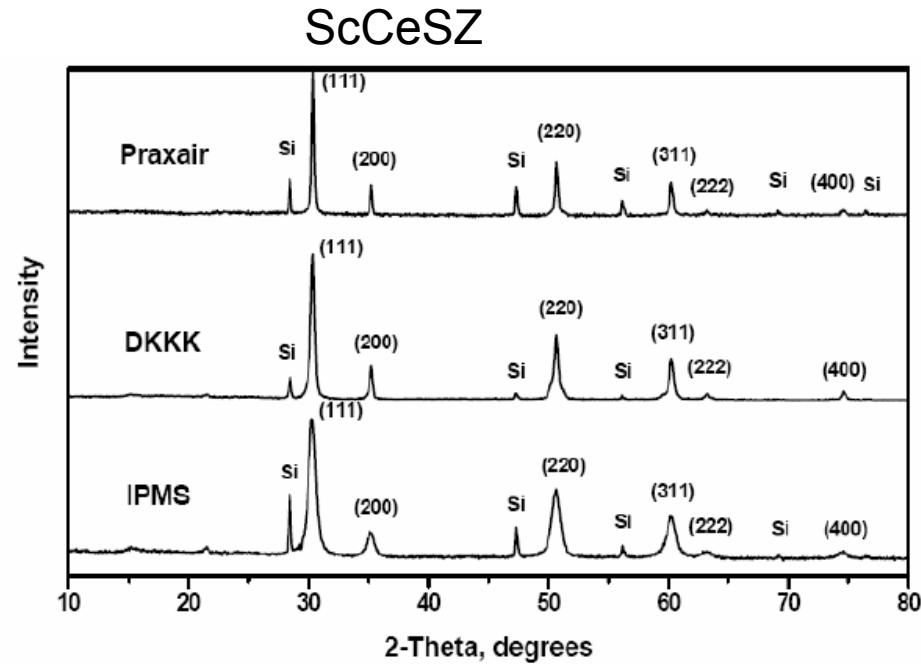
ScCeSZ

LSM+ScCeSZ

New phases are absent in LSM-ScCeSZ nanocomposites

LSM-ScCeSZ

Sintering T_c (°C)	Fluorite		D XRD, nm	Perovskite		
	D XRD, nm	Lattice parameter (Å)		Lattice parameter (Å)		
		a		a		c
700	12.6	5.0927	32.8	5.499		13.365
900	23.5	5.0965	48.0	5.513		13.378
1100	52.3	5.0990	70.5	5.526		13.381

Nanodomains. LSM and ScCeSZ parameters increase with sintering T due to La incorporation into F and Sc/Zr incorporation into B positions of P
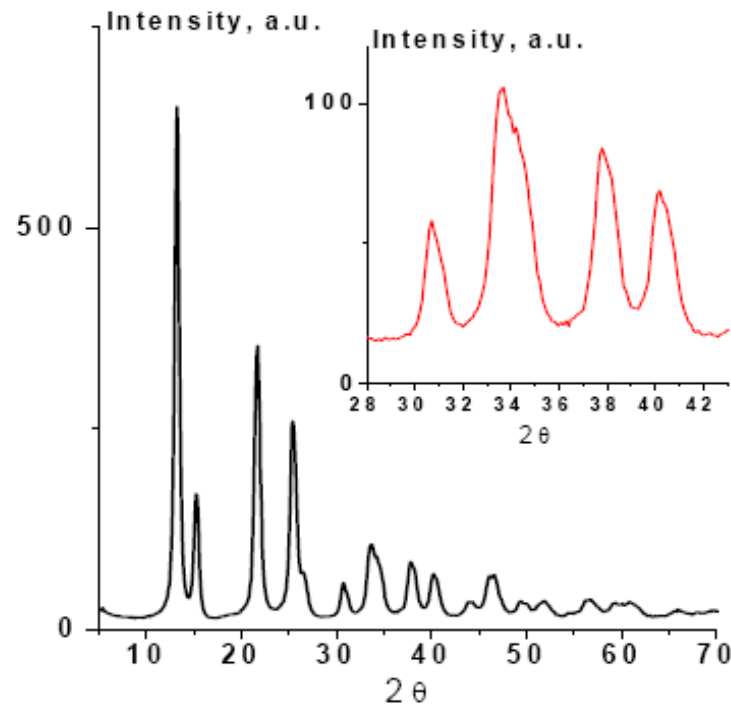
Detection of new phases during sintering
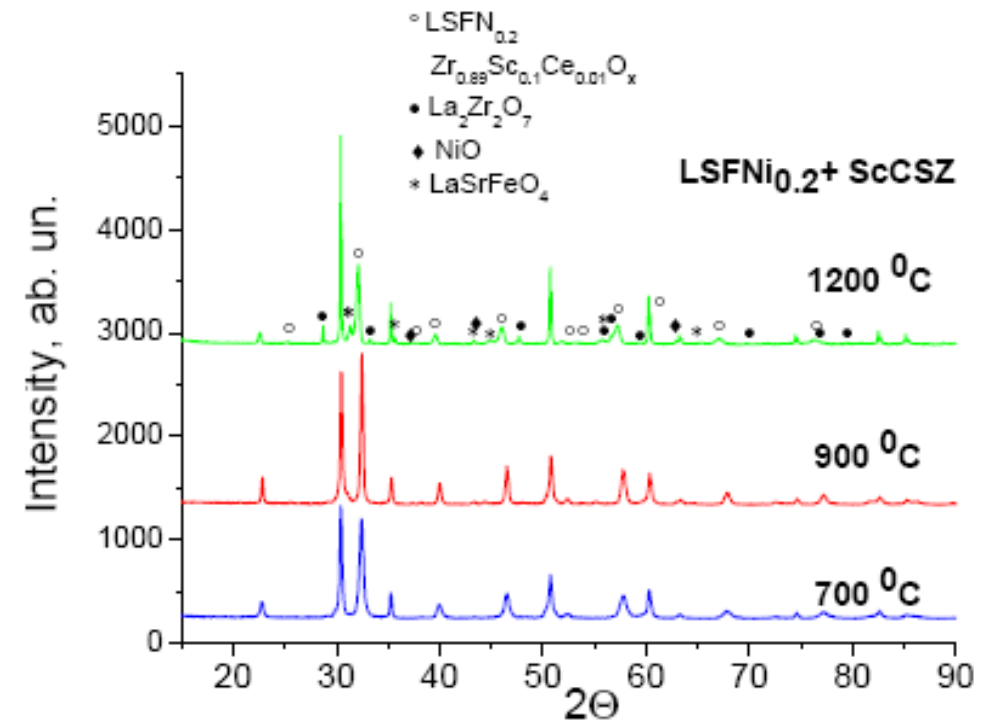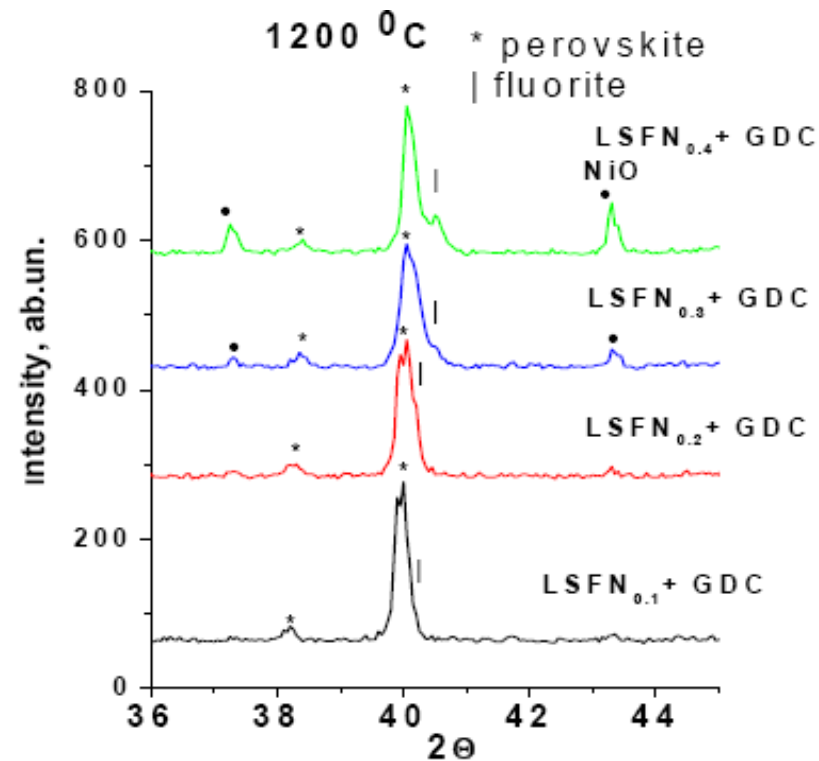
Segregation of NiO phase from LSFN –GDC nanocomposite
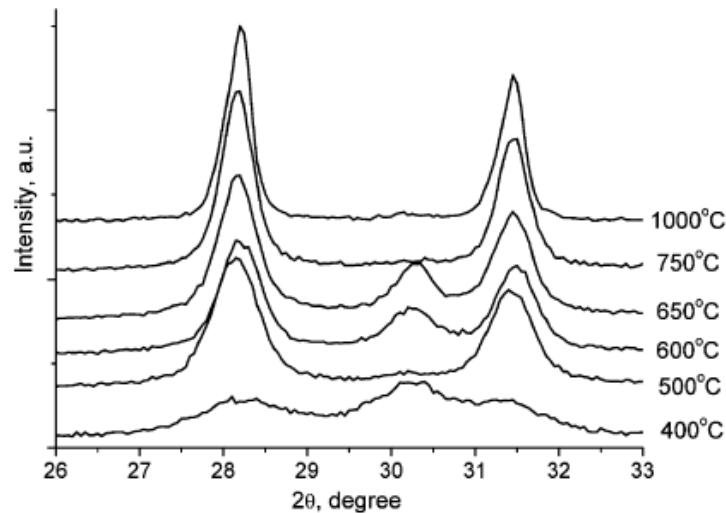Formation of pyrochlore $La_2Zr_2O_7$ phase in LSFN-ScCeSZ nanocomposite

XRD on Synchrotron Radiation (SR)

XRD pattern of $Ce_{0.5}Zr_{0.5}O_2$ at $\lambda=0.703$ Å

Strong asymmetry of diffraction peaks due to coexistence of domains enriched either by Ce or Zr cations

Modeling XRD patterns: ZrO_2 case

Experimental (1) and simulated diffraction pattern (2) for sample calcined at 650 °C

Experimental diffraction patterns of zirconia samples from Zr hydroxide calcined at different temperatures
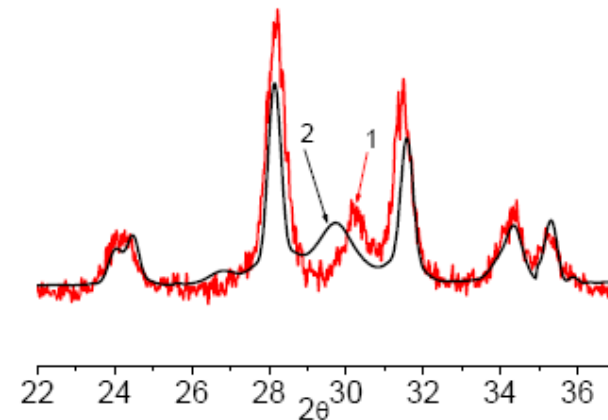
Modeling of the X-ray diffraction patterns for multiply twinned nanoparticles of monoclinic phase as revealed by TEM. The structure of the monoclinic phase can be considered as comprised of alternating layers of oxygen and zirconium layers situated along the (001) plane. In modeling, the crystallites were considered as formed by stacked alternating slabs with a mirror symmetric structure $\Rightarrow$ appearance of fragments with a structure of c-ZrO_2 (peak at $2\theta \sim 30.2°$)

Neutron Powder Diffraction (NPD): $Ce_{1-x}Pr_xO_{2-\delta}$

Typical diffraction pattern and its fitting
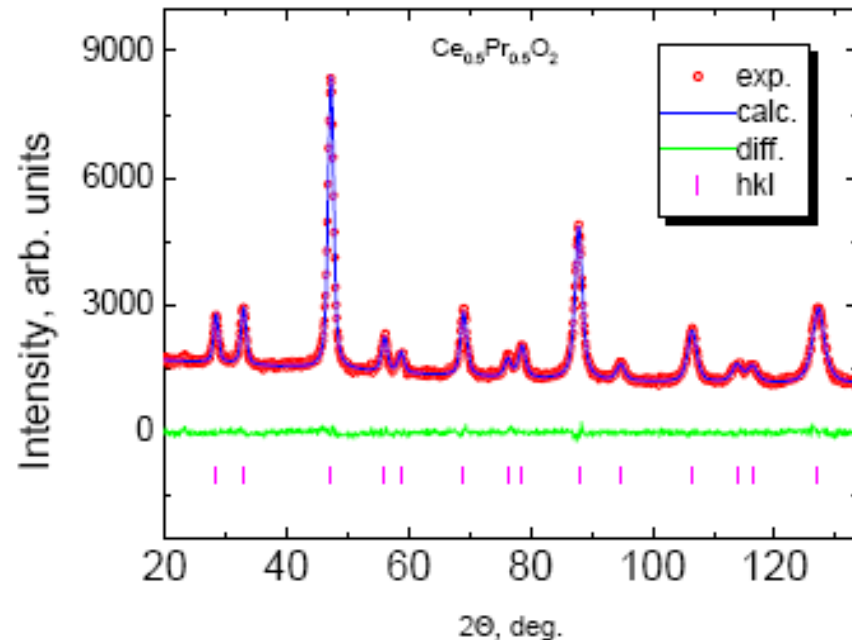
Angle dependence of peaks HW
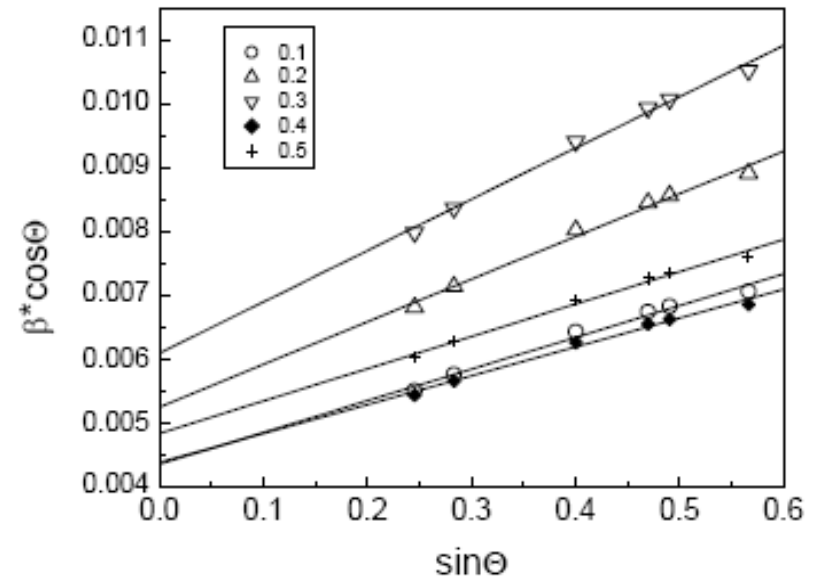
NPD is sensitive to oxygen anions, so allows to estimate disordering of anion sublattice
Angle dependence analysis allows to estimate separately domain sizes and microstrains density
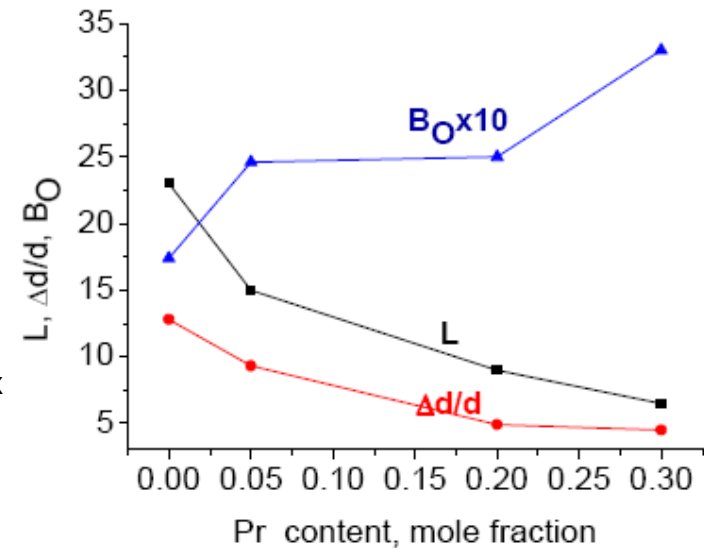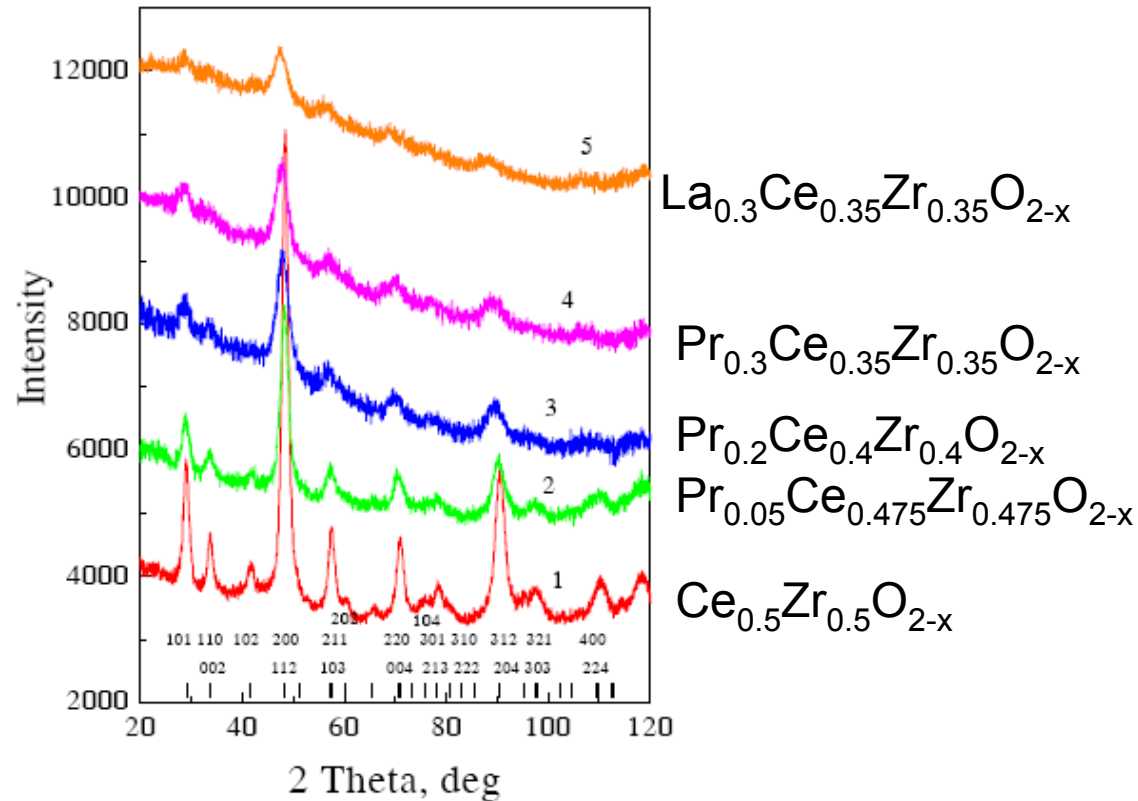
NPD: detailed characteristics of real structure

Табл.1. Structural parameters, interatomic distances, microstrain density, particle size and intensity of diffuse scattering for $Ce_{1-x}Pr_xO_2$ samples*

Pr content, x	0	0.1	0.2	0.3	0.4	0.5
a, Å	5.4108(2)	5.4159(7)	5.4199(8)	5.421(1)	5.4128(6)	5.4120(7)
B, Å^{-2} Ce/Pr	0.04(4)	0.11(5)	0.21(5)	0.34(6)	0.23(5)	0.29(5)
O	0.12(4)	0.41(4)	0.48(4)	0.57(5)	0.48(4)	0.60(4)
L(Ce-O), Å	2.3430(1)	2.3451(2)	2.3469(2)	2.3472(3)	2.3438(2)	2.3435(2)
(O-O), Å	2.7054(1)	2.7079(4)	2.7099(4)	2.7104(5)	2.7064(3)	2.7060(4)
χ^2	2.33	1.54	1.54	1.28	1.62	1.52
R_p	3.26	2.24	1.83	1.74	2.46	2.35
R_{wp}	4.21	2.86	2.34	2.20	3.14	2.99
R_{Br}	1.71	2.20	2.71	2.26	2.58	1.68
R_f	1.02	1.43	1.77	1.50	1.64	1.03
Microstrains		0.00497	0.00668	0.00804	0.00452	0.00506
Particle size, nm		35	30	25	35	32
Intensity of diffuse scattering, rel. un	850	1650	2540	2410	1350	1370

* Space group Fm3m.. B - isotropic temperature parameter for the atom. R_p, R_{wp}, R_b and R_f - the conventional factors which show the quality of the agreement between observed and calculated data.

NPD for $Ln_x(Ce_{0.5}Zr_{0.5})_{1-x}O_{2-\delta}$

$La_{0.3}Ce_{0.35}Zr_{0.35}O_{2-x}$

$Pr_{0.3}Ce_{0.35}Zr_{0.35}O_{2-x}$

$Pr_{0.2}Ce_{0.4}Zr_{0.4}O_{2-x}$

$Pr_{0.05}Ce_{0.475}Zr_{0.475}O_{2-x}$

$Ce_{0.5}Zr_{0.5}O_{2-x}$

Intensity

2 Theta, deg

$B_O \times 10$

L, $\Delta d/d$, B_O

L

$\Delta d/d$

Pr content, mole fraction

Disordering of oxygen sublattice is reflected in thermal parameter B_o
Peaks broadening is determined by decreasing domain sizes L with Pr content
Microstrains density $\Delta d/d$ decreases with doping due to more uniform distribution
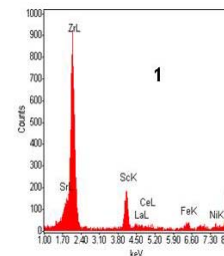of Ce and Zr between neighboring domains

WAXS

Radial distribution function curves for ceria-zirconia samples
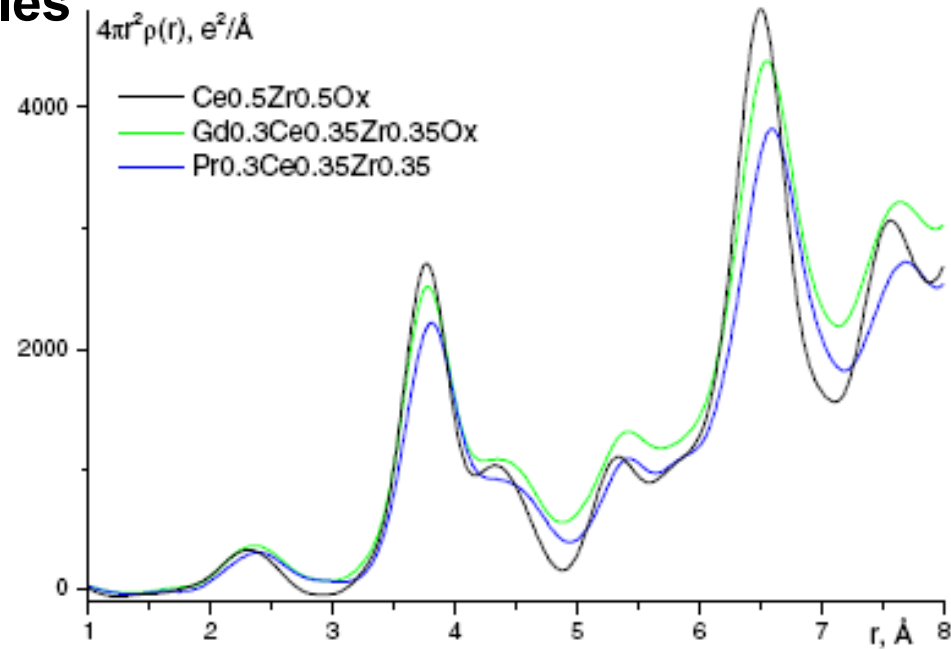
Peak position determined by distances in the cell, area –by coordination numbers

LSNF+GDC

700°C — 100 nm

900°C — 100 nm

1100°C — 100 nm
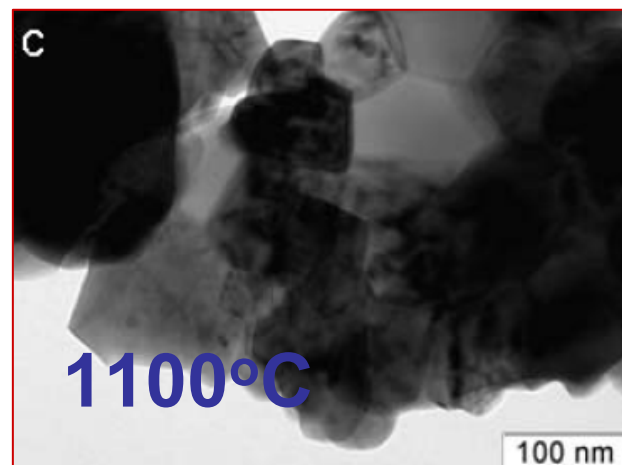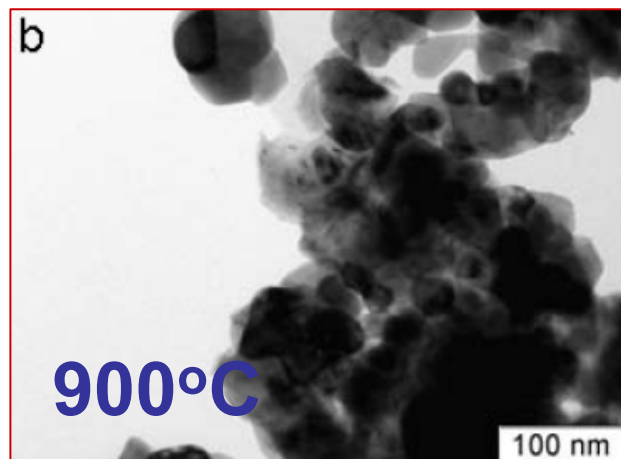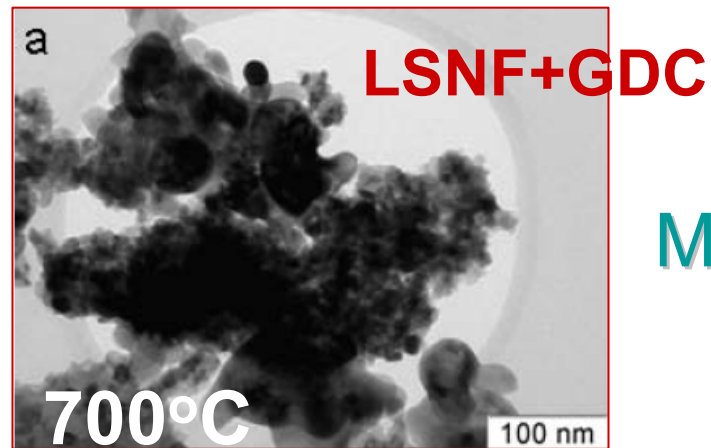
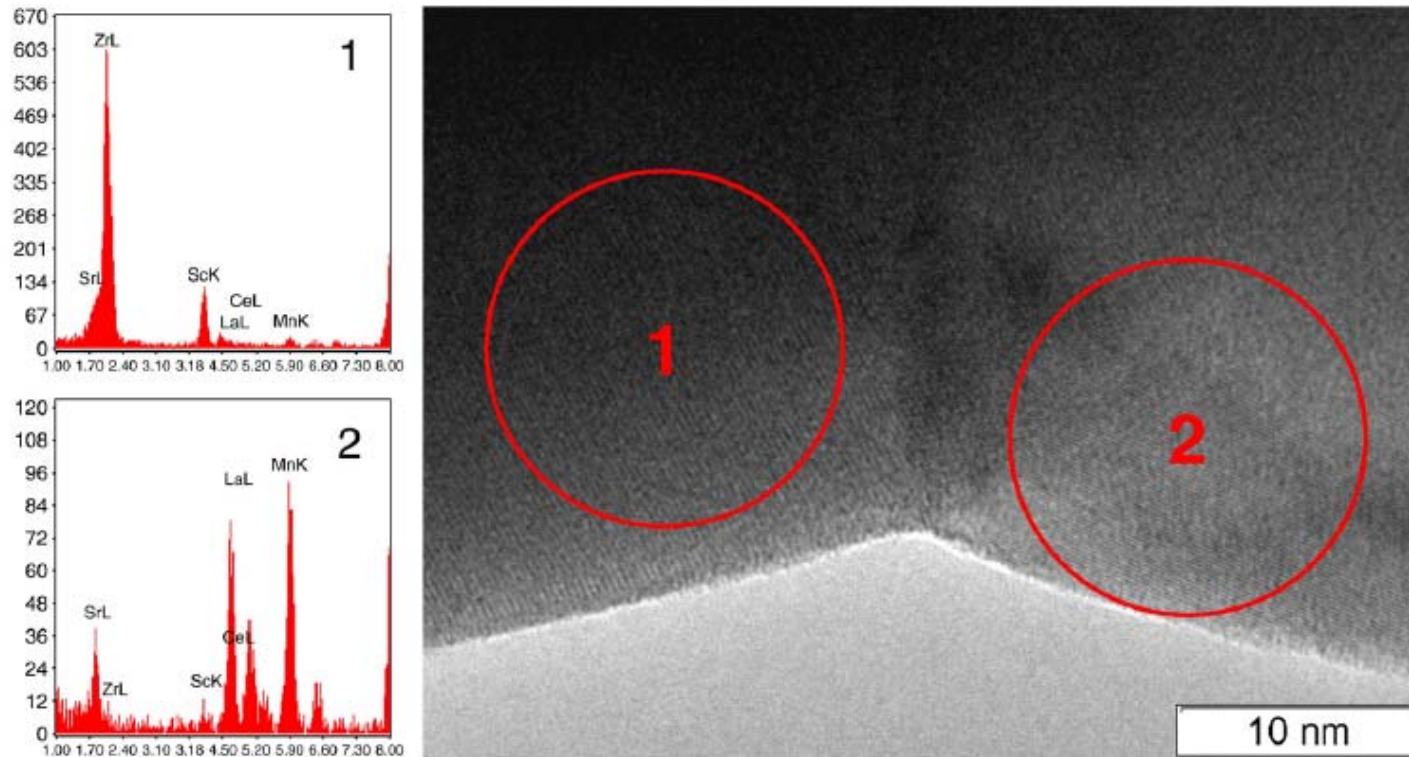Microstructure of cathode materials by Transmission Electron Microscopy (TEM)
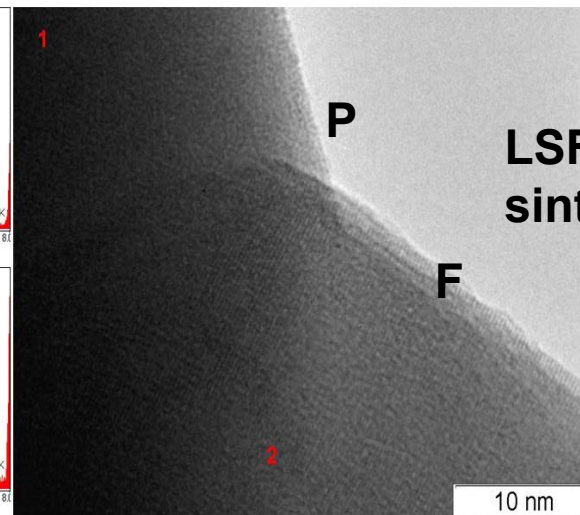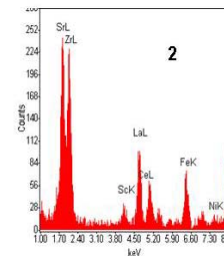
$LSFNi_{0.2}$-ScCeSZ sintered at 1200 °C

P
F

Coherent P-F domains stacking

Uniformly intermixed particles of both phases, A lot of P-electrolyte interfaces
Annealing pores with $T_{sint.}$, more interfaces

TEM with EDX-local elemental analysis

EDX spectra of neighboring fluorite (1) and perovskite (2) domains in LSM–ScCeSZ composite sintered at 1100 °C.

<u>Observed lattice spacing</u>: 2.55 Å—(200) planes of $Sc_{0.2}Ce_{0.01}Zr_{0.79}O_{2-\delta}$ (1) and 1.58 Å—(132) planes of $La_{0.8}Sr_{0.2}MnO_3$ (2).

<u>Domain composition</u> : $La_{0.07}Sr_{0.07}Sc_{0.16}Ce_{0.006}Mn_{0.04}Zr_{0.73}O_{2-\delta}$ (1) and $La_{0.73}Sr_{0.16}Sc_{0.02}Zr_{0.014}MnO_{3+\delta}$ (2).

Redistribution of elements between domains of perovskite and electrolyte

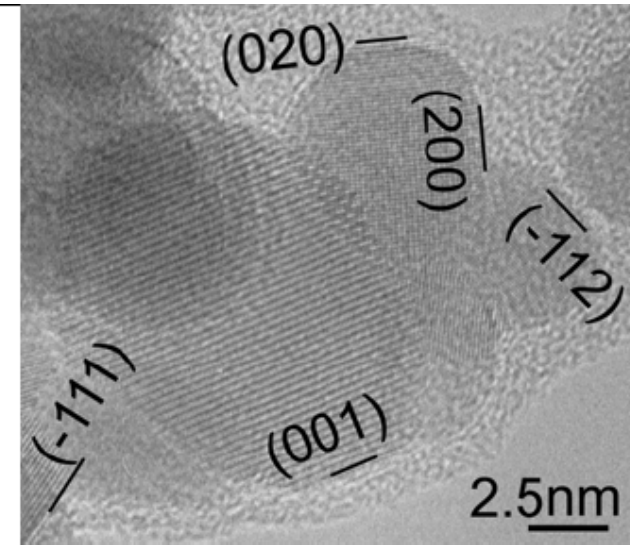# TEM to assess surface planes in nanoparticles: ZrO$_2$ case
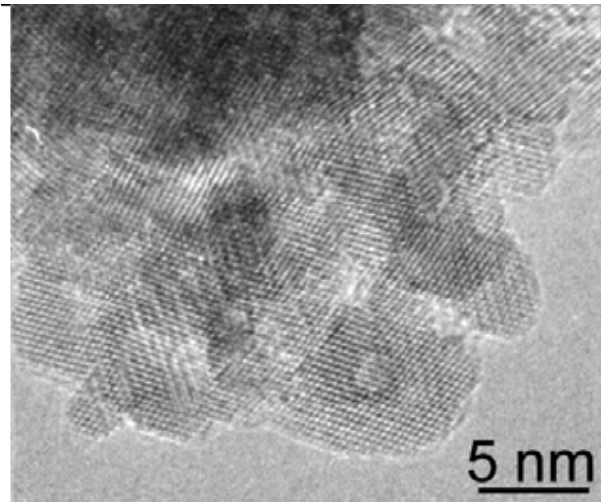
Aggregates of oriented m-ZrO$_2$ nanoparticles (a) and corresponding digital diffraction pattern (DDP) with reflections shown by arrows
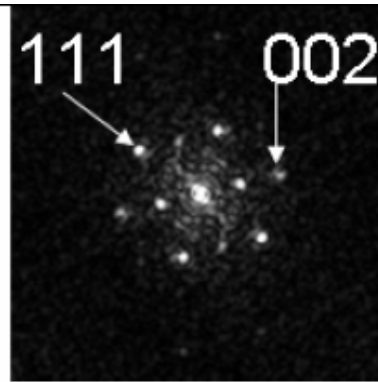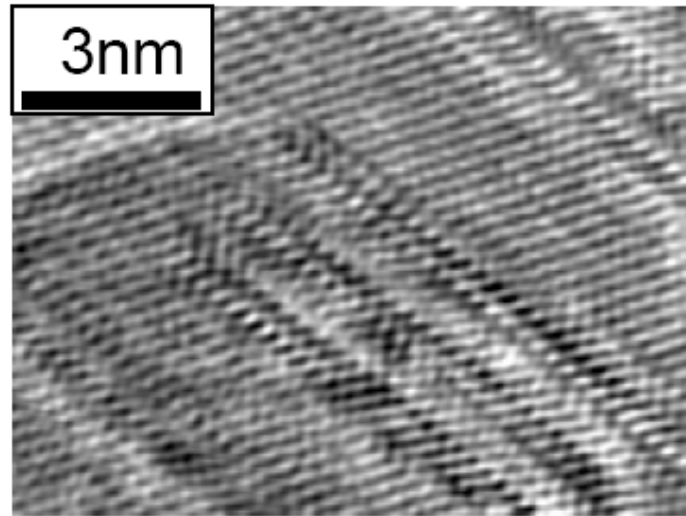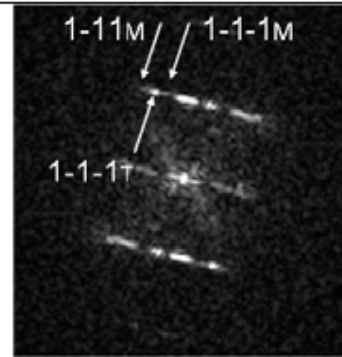
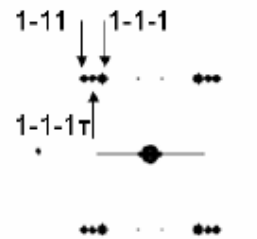Rounded particles of m- ZrO$_2$ in sample calcined at 500 ^{o}C; the types of surface faces are indicated.
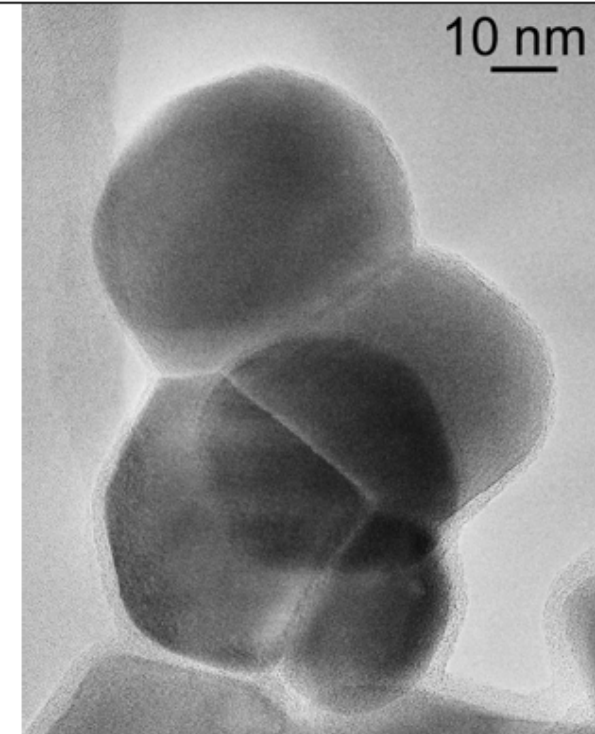
TEM to detect extended defects: ZrO_2 case

HRTEM image of the multiply twinned particle with a small (~1 nm) distance between twinning planes (a); DDP from this region in [110] projection (b) and its modeling for the mixture of m- and t-phases (c).

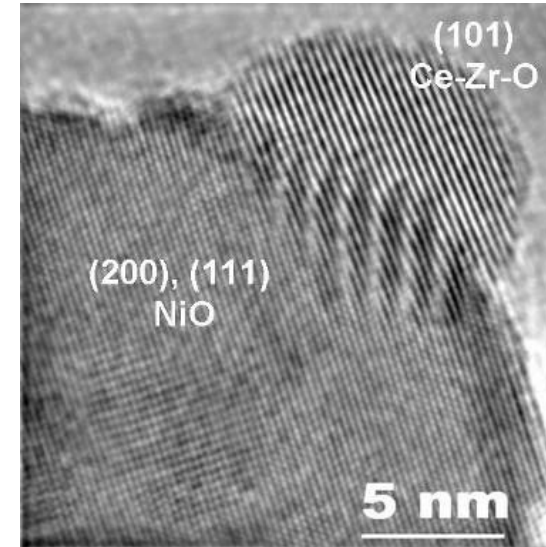TEM image of the particle of 1000 ^oC sample with separate twins visible.

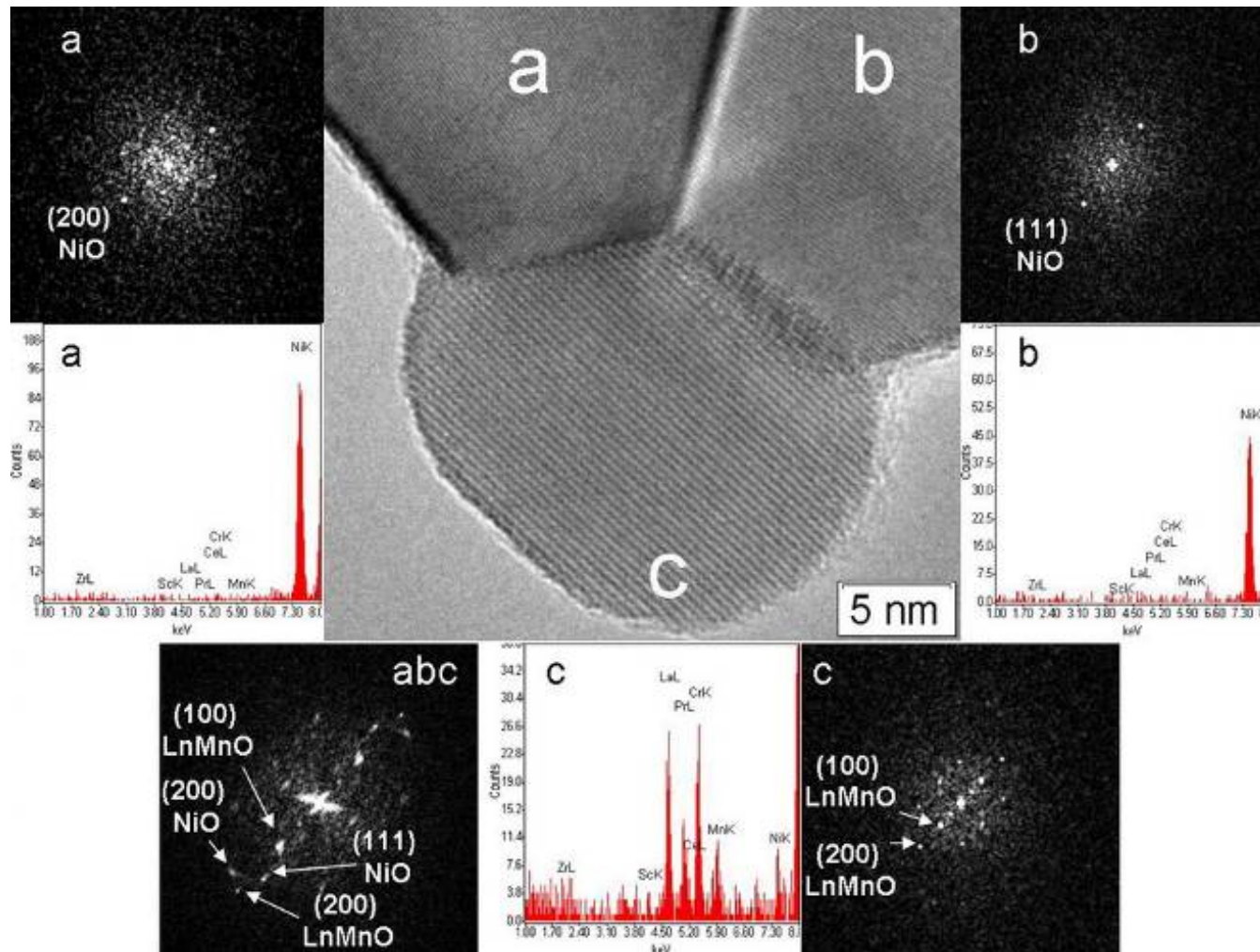# Microstructure by TEM: promoted anode materials

Perovskite LaPrMnCrO layers on NiO
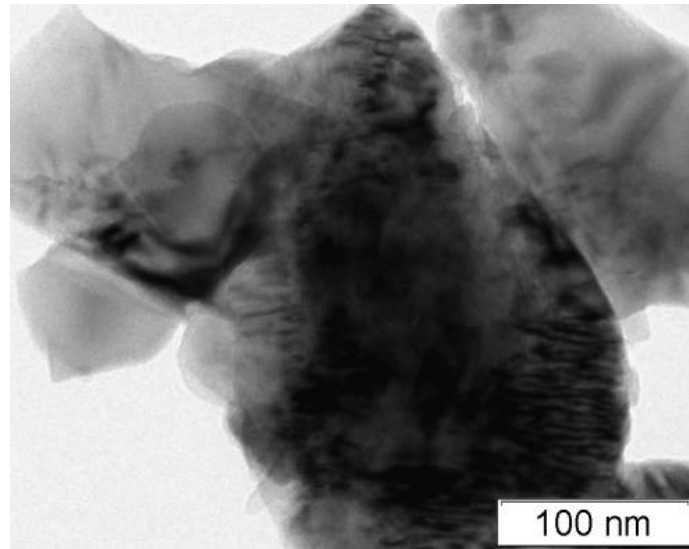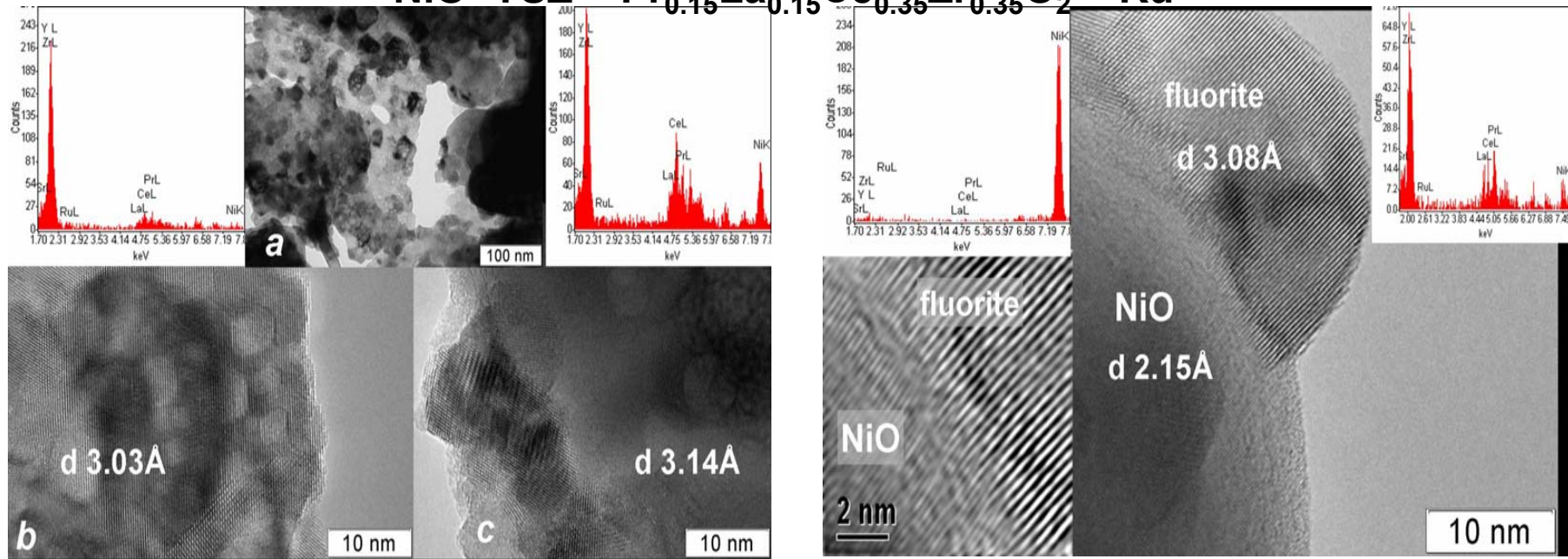
Fluorite layers on NiO

Good decoration and epitaxy required to prevent coking in CH_4 steam reforming

Microstructure by TEM: doped anode materials

Coherently stacked perovskite LnMnCrO and NiO domains

Microstructure by TEM:doped anode materials

NiO+YSZ + $Pr_{0.15}La_{0.15}Ce_{0.35}Zr_{0.35}O_2$ + Ru


a- macro/mesoporous aggregates of particles;

b-disordered nanodomain ZrO_2 particle containing internal nanopores and respective EDX spectrum;

c –disordered nanodomain particles of fluorite-like oxide promoter on the surface of NiO particle and respective EDX spectrum;

d-contact area between NiO and YSZ particle modified by the elements of complex oxide promoter.

$\Rightarrow$ strong interaction between all phases of anode composite material with redistribution of components between phases

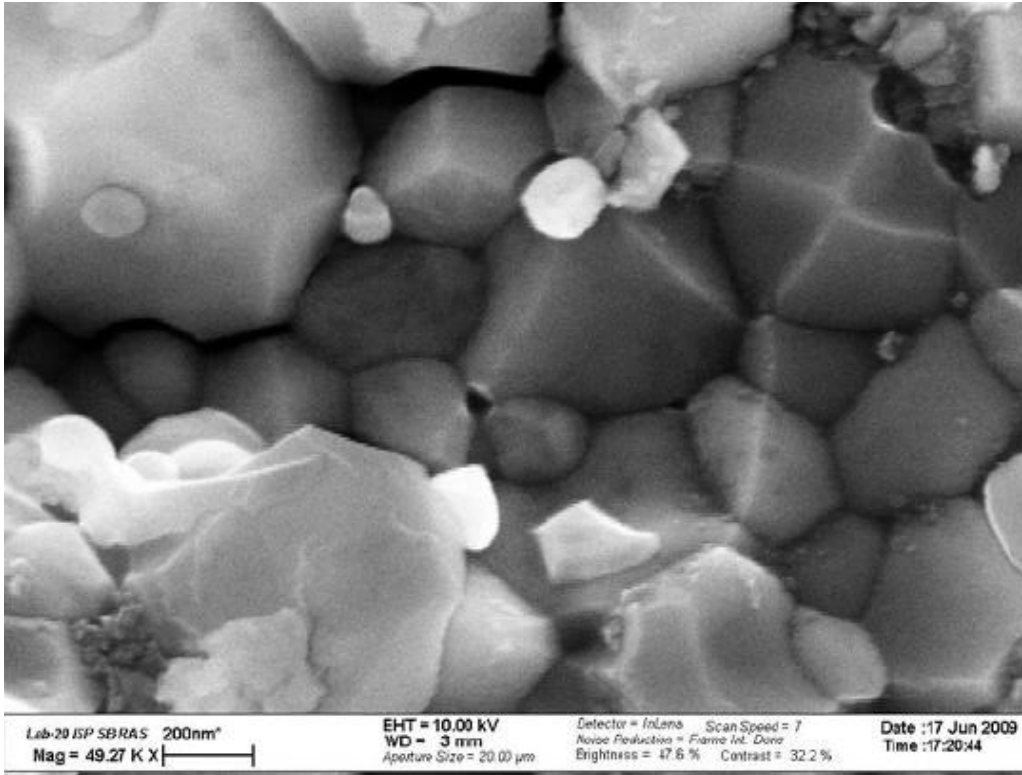# SEM: density and crystallinity of electrolyte layers

$$La_{9.83}Si_{4.5}Fe_{1.5}O_{26\pm\delta}$$
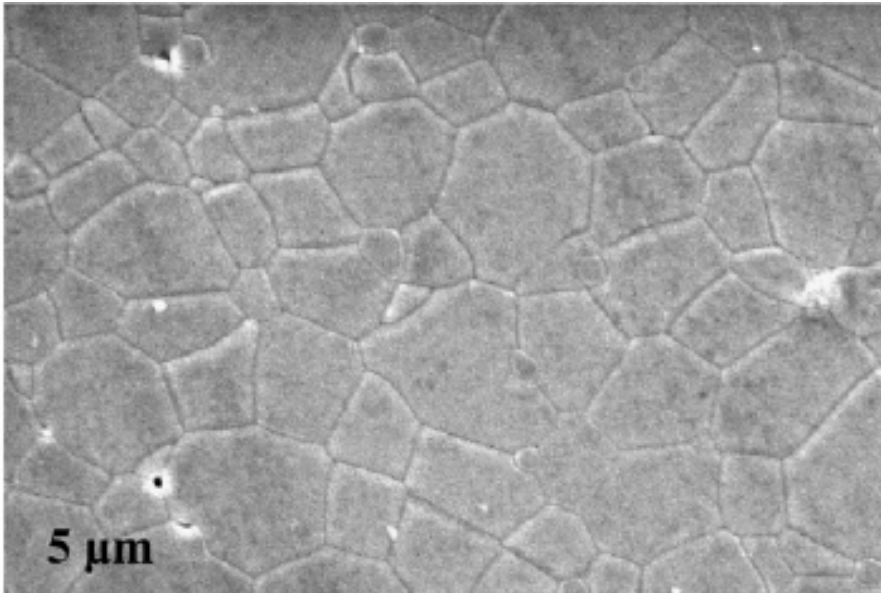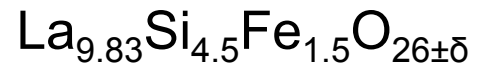
Conventional sintering 1500 ºC
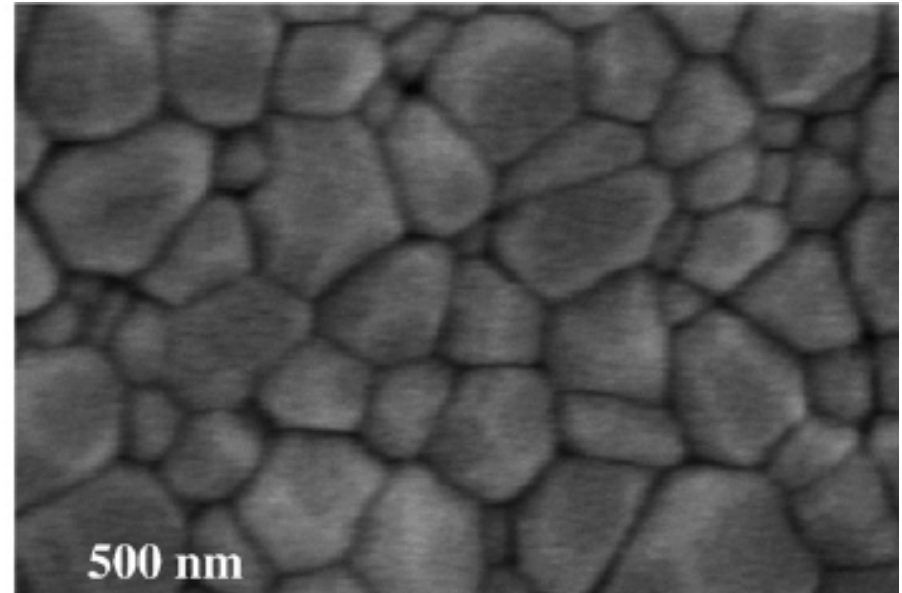
Spark-plasma sintering 1100 ºC.

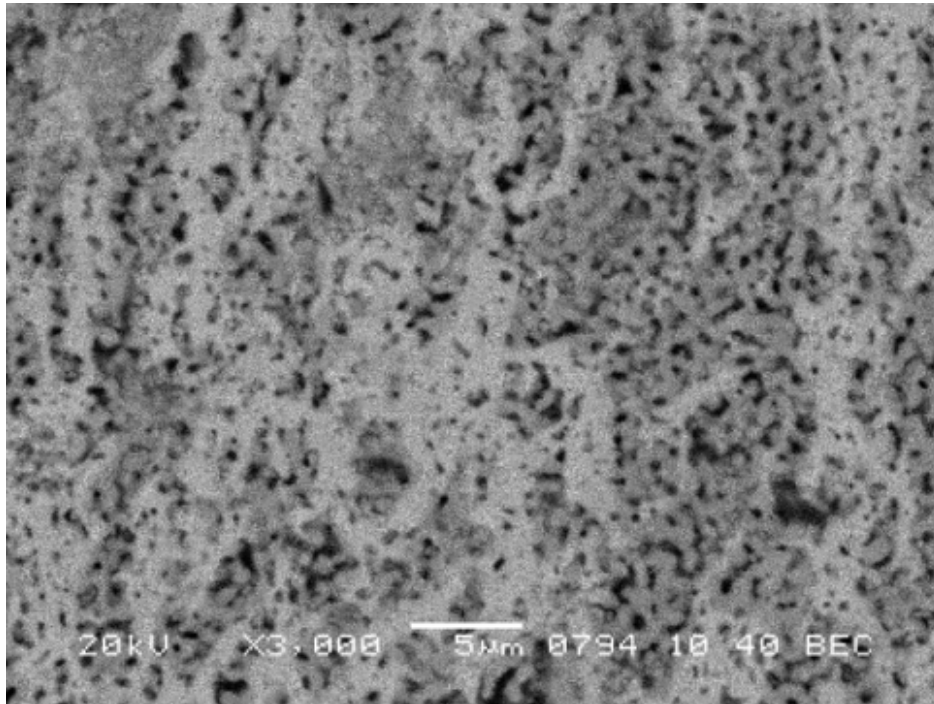Much smaller domain sizes in ceramics sintered by advanced techniques

SEM: cathode nanocomposites

SEM image of the cleaved surface of LSFN-GDC pellet sintered at 1200 $^{\circ}$C.

Surprising crystallographic ordering of interfaces, each detected particle is comprised of smaller P+F domains, could favor fast oxygen diffusion
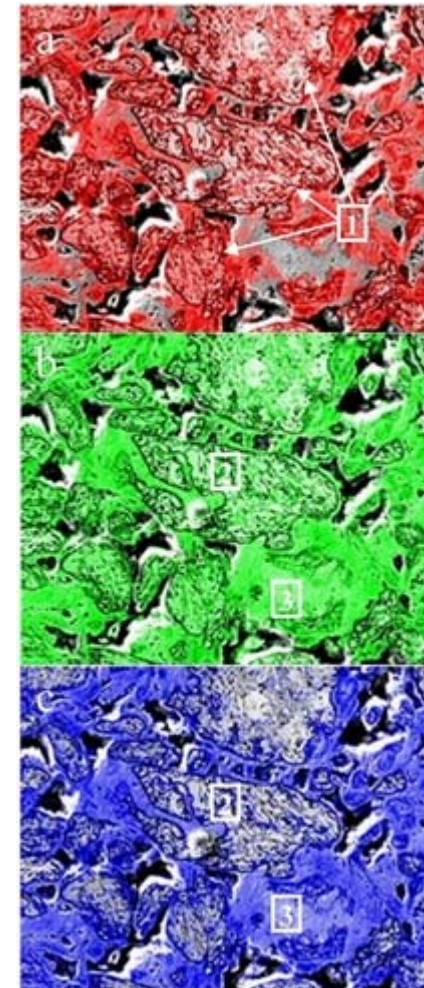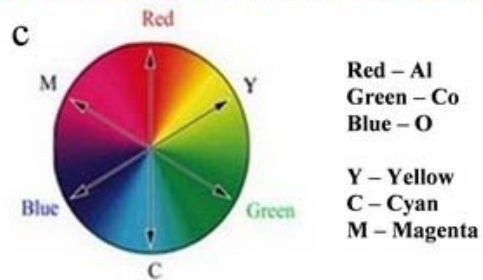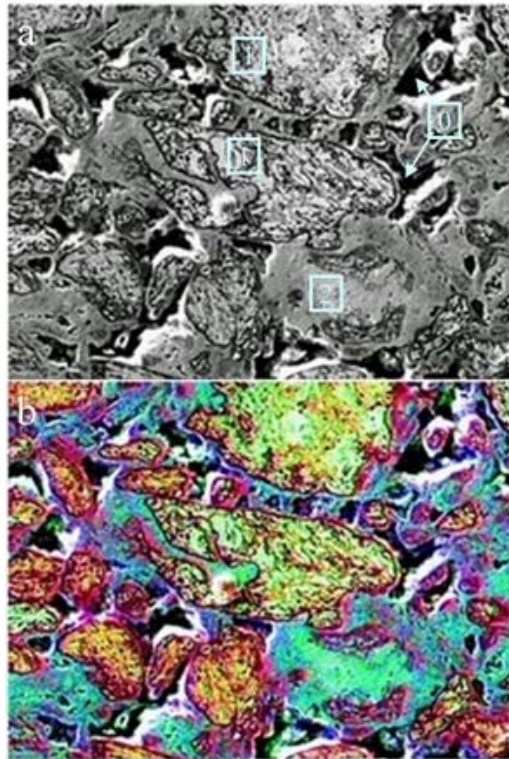
SEM in scattered electrons

$LaFe_{0,7}Ni_{0,3}O_3$ (50%) – $Ce_{0,9}Gd_{0,1}O_2$ (50%)

Control of uniformity of spatial distribution and percolation of ionic or electronic-conducting phases

SEM: elements spatial distribution in nanocomposites

Element distribution maps of Al (a), Co (b), O (c) from cermet surface superimposed on SEM micrograph; 1 – alumina shell which encapsulates the metallic core; 2 – oxygen-free cores; 3 – high oxygen concentration matrix.
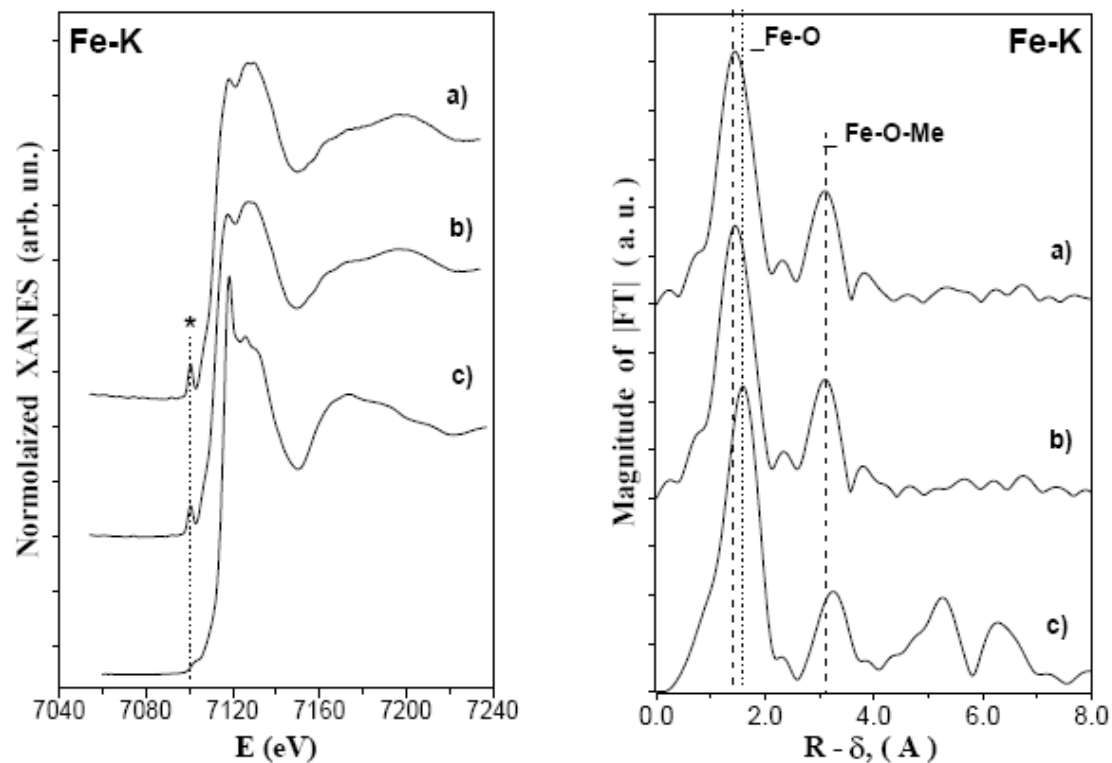
SEM: identification of surface phases by superposition of elemental maps
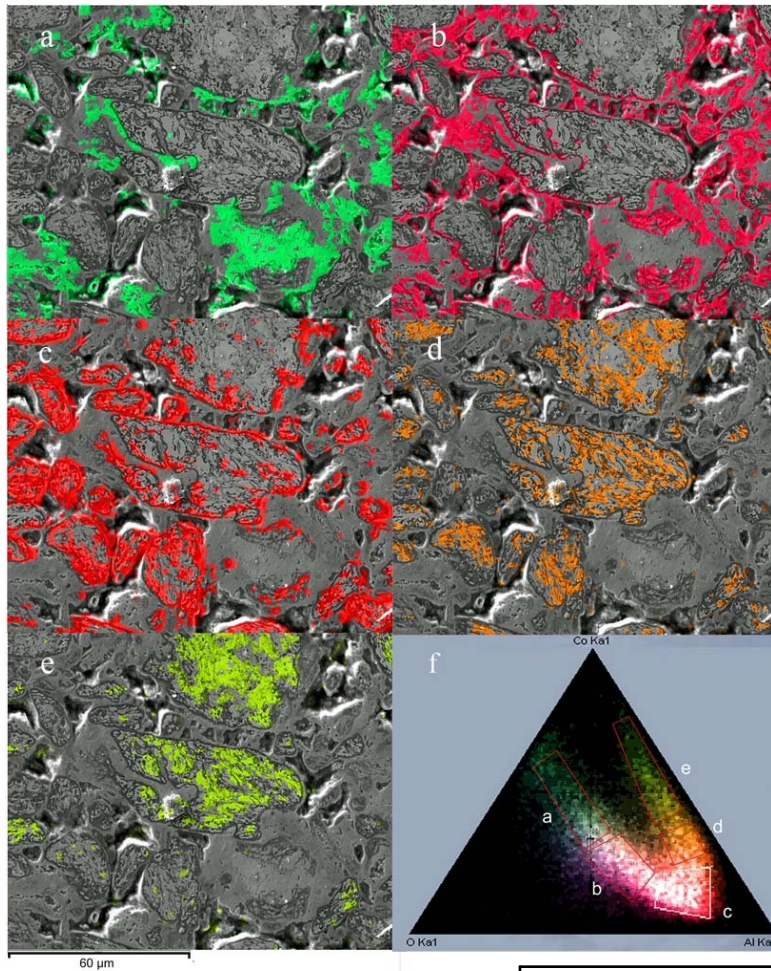
Composition of different fragments

Fragments in Fig. 12	O, at. %	Al, at. %	Co, at. %
a (emerald)	45.1	9.3	45.5
b (scarlet)	52.7	23.5	23.8
c (red)	42.2	39.8	18.1
d (orange)	20.1	36.7	43.2
e (green)	11.5	24.8	63.7

# EXAFS: analysis of fine structure of X-ray absorption edges caused by scattering of emitted electrons

Allows to estimate distances and coordination numbers in different lattice positions

XANES spectra (Fe-K edge)(left) and radial distribution function curves (right) describing Fe local arrangement for samples: a - $La_{10}Si_4Fe_2O_{26}$, b - $La_{9.83}Si_{4.5}Fe_{1.5}O_{26}$, c -$LaFeO_3$.
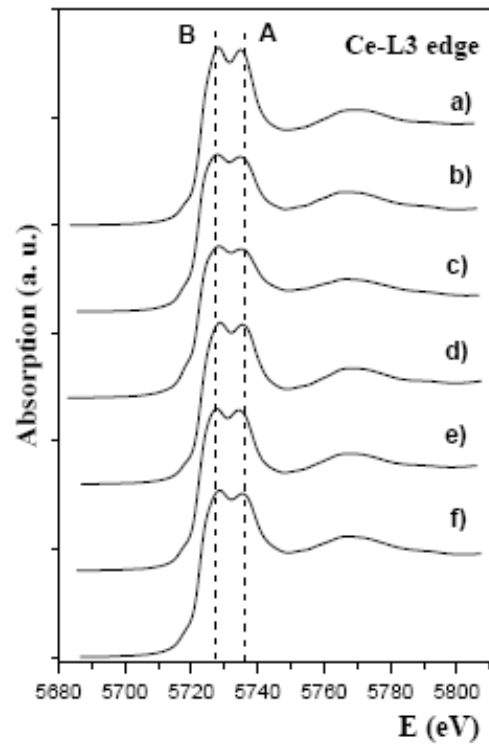
Tetrahedral coordination of Fe^{3+} cations in La silicates and octahedral in perovskite
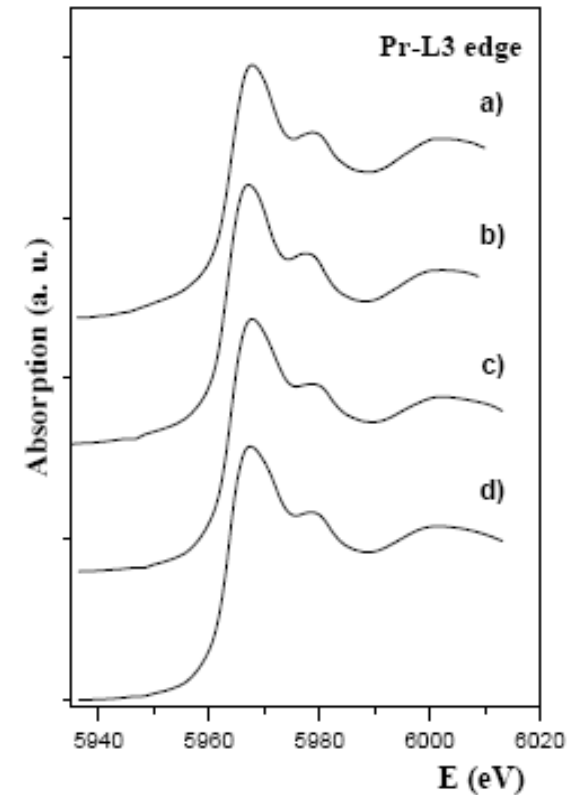
EXAFS: effect of ceria doping on local structure
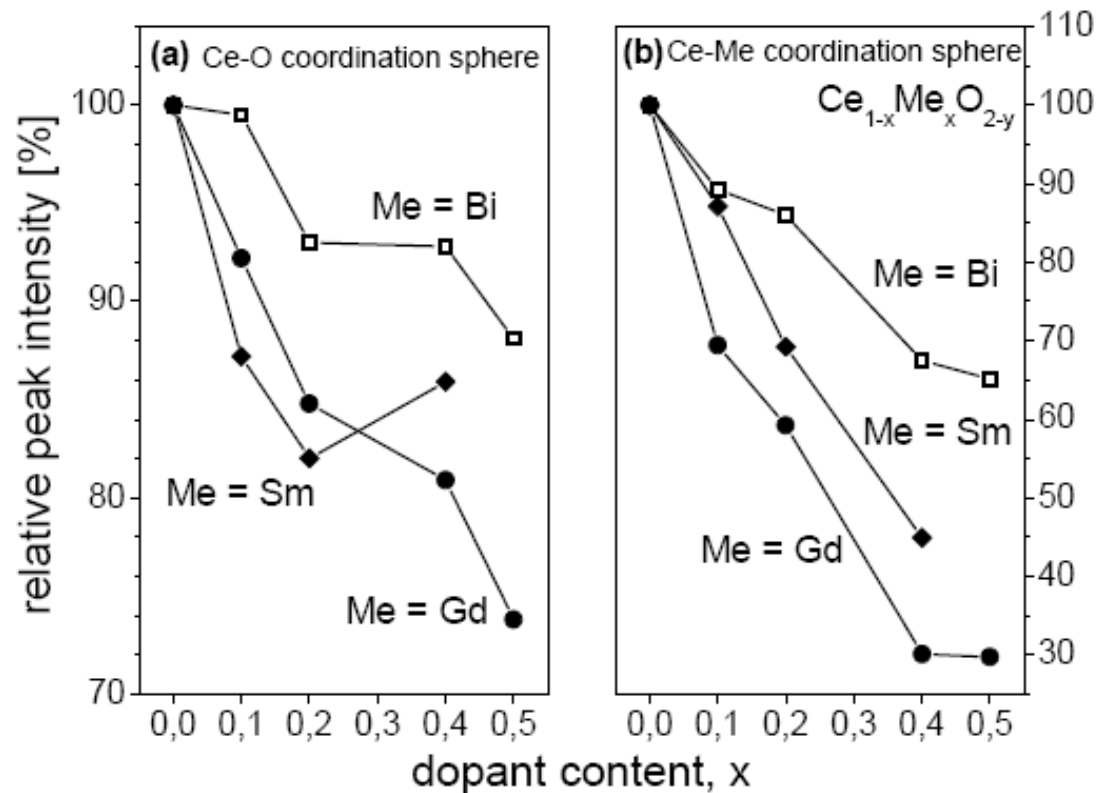
Decline Ce-O CN with doping level ⇒ rearrangement of coordination polyhedra, not simple generation of randomly distributed anion vacancies

XANES: charge state

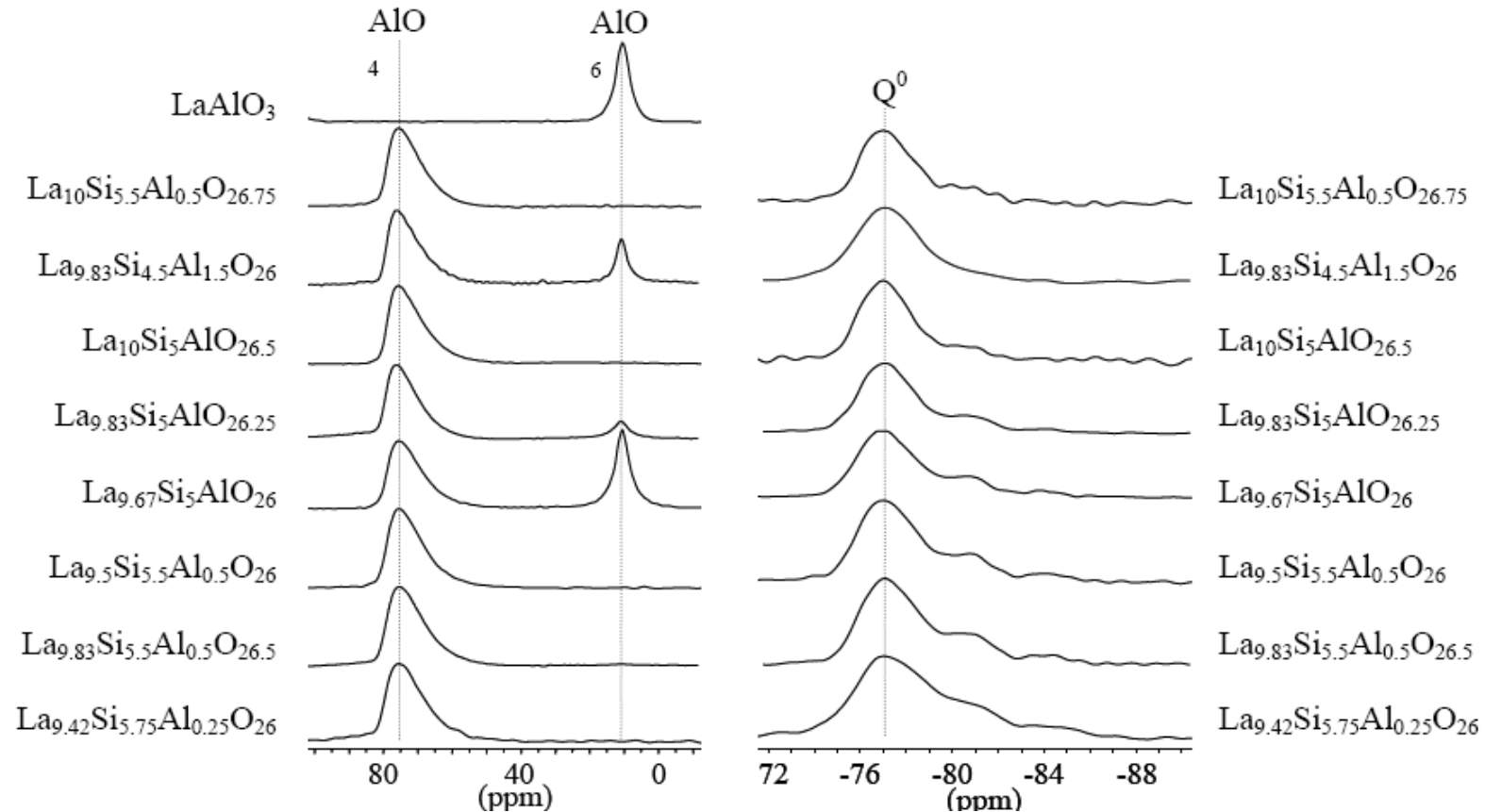

Pr content 0, 10, 20, 30, 40 and 50 at. %

Pr content 20, 30, 40 and 50 at. %

Ce in 4+ state, Pr in both 3+ and 4+ state

Nuclear Magnetic Resonance (NMR)

^{27}Al (left) and ^{29}Si (right) MAS NMR spectra of Al-doped systems

Band position depends on oxygen coordination sphere. Al in substitution position in apatite structure –in Td, in $LaAlO_3$ admixture - in Oh
Along with ideal isolated SiO_4 units (Q^o), condensed Si-O-Si groups are revealed by bands at more negative chemical shifts

UV-Vis: charge state and coordination of cations (d-d transitions), Me-O strength (charge transfer bands)
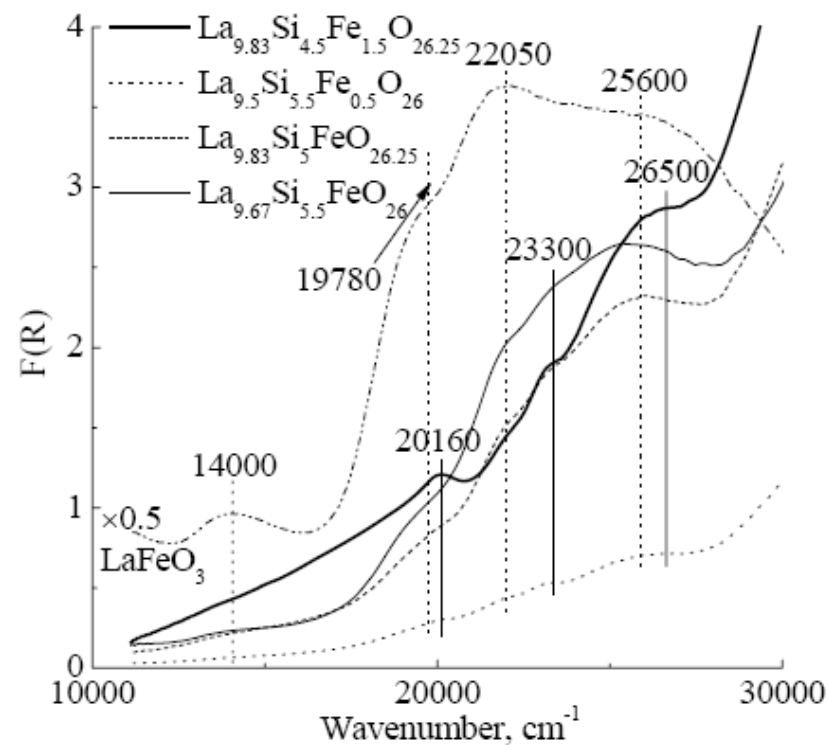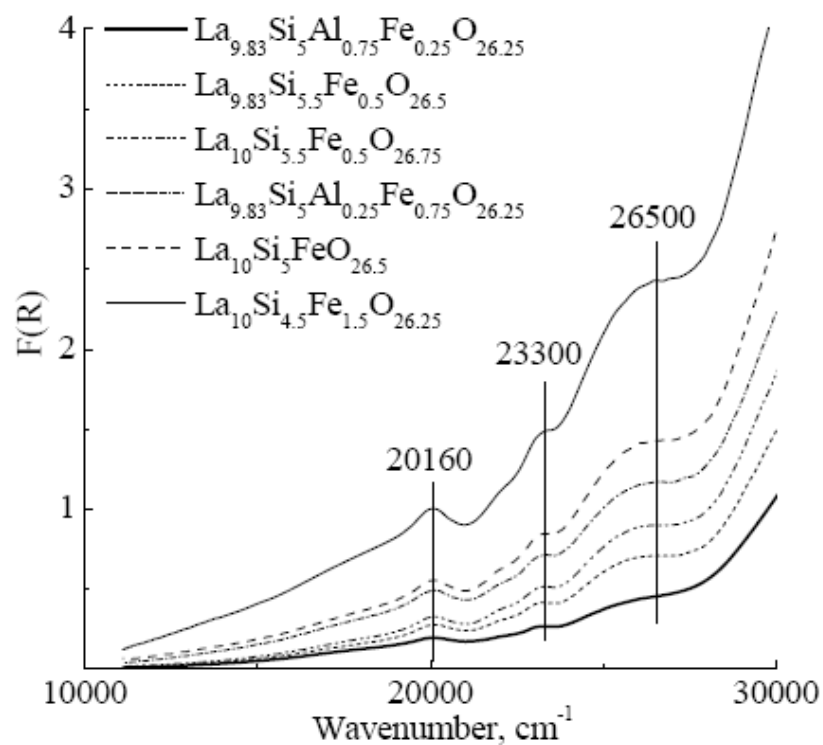
Fe^{3+}_{Td} in substitution positions of apatites + admixture of $LaFeO_3$

UV-Vis for doped ceria
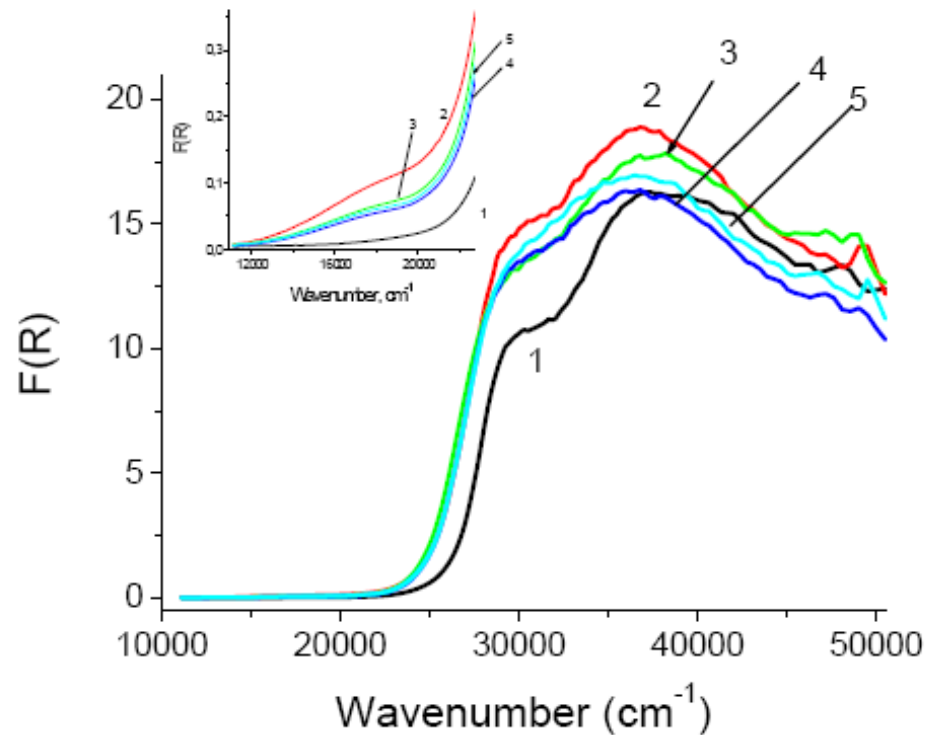
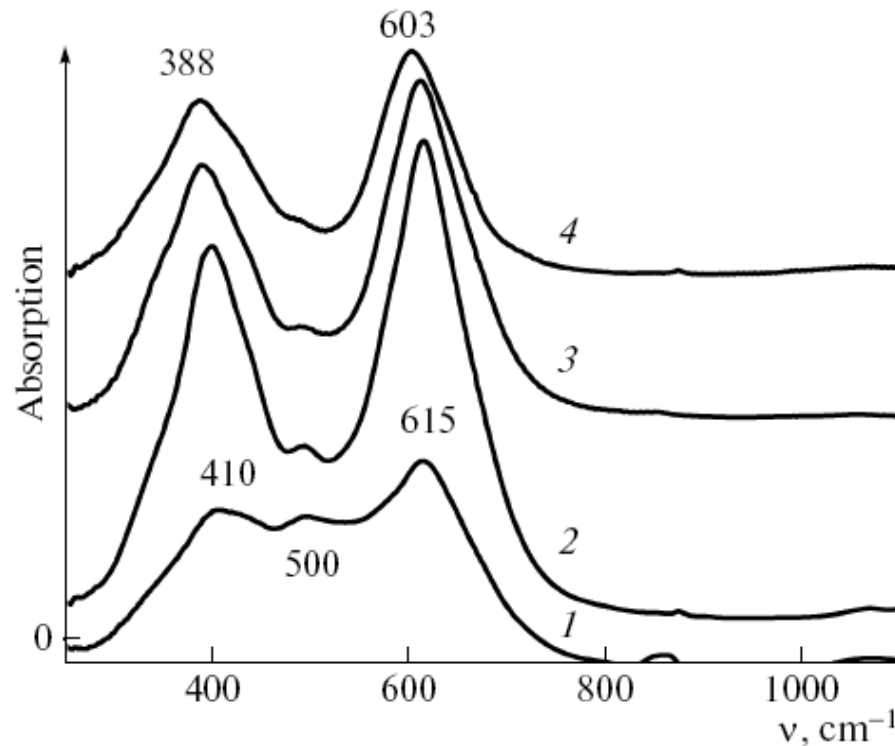UV-Vis spectra of CeO_2 (1) and $Ce_{1-x}Sm_xO_{2-\delta}$ at x=0.05 (2), 0.1 (3), 0.15 (4) and 0.2 (5)

Shift of CTB to lower wave numbers with doping suggests deformation of coordination polyhedra leading to appearance longer Me-O distances

FTIRS of lattice modes: perovskites

IR spectra of (1) $LaMnO_{3.40}$, (2) $LaMnO_{3.24}$, and (3) $LaMnO_{3.19}$, and (4) after removal of a 0.5 monolayer of oxygenby thermodesorption in a helium flow at 650°C.
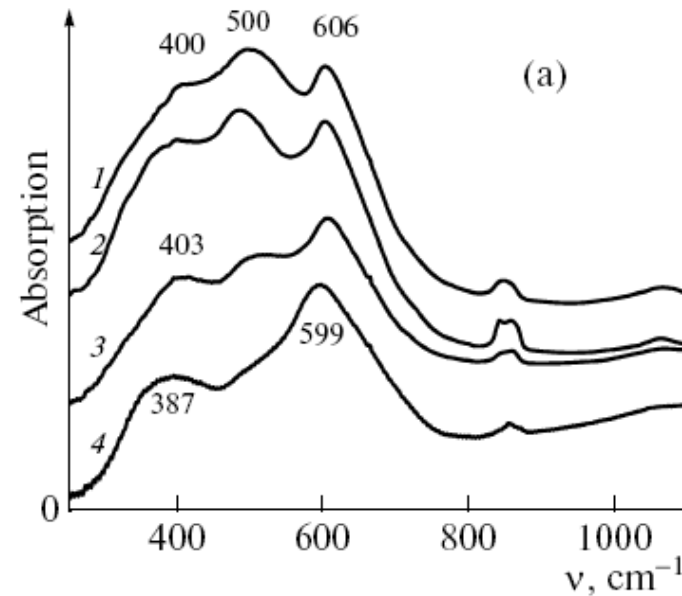
(1) LaCeMn, (2) LaFeMn, (3) LaBiMn, and (4) LaSrBiMn calcined at 500 C

Number of bands is determined by the local symmetry of the lattice.
Strong distortion in low-temperature manganites due to cation vacancies: band at ~ 500 cm⁻¹

FTIRS of lattice modes: apatites
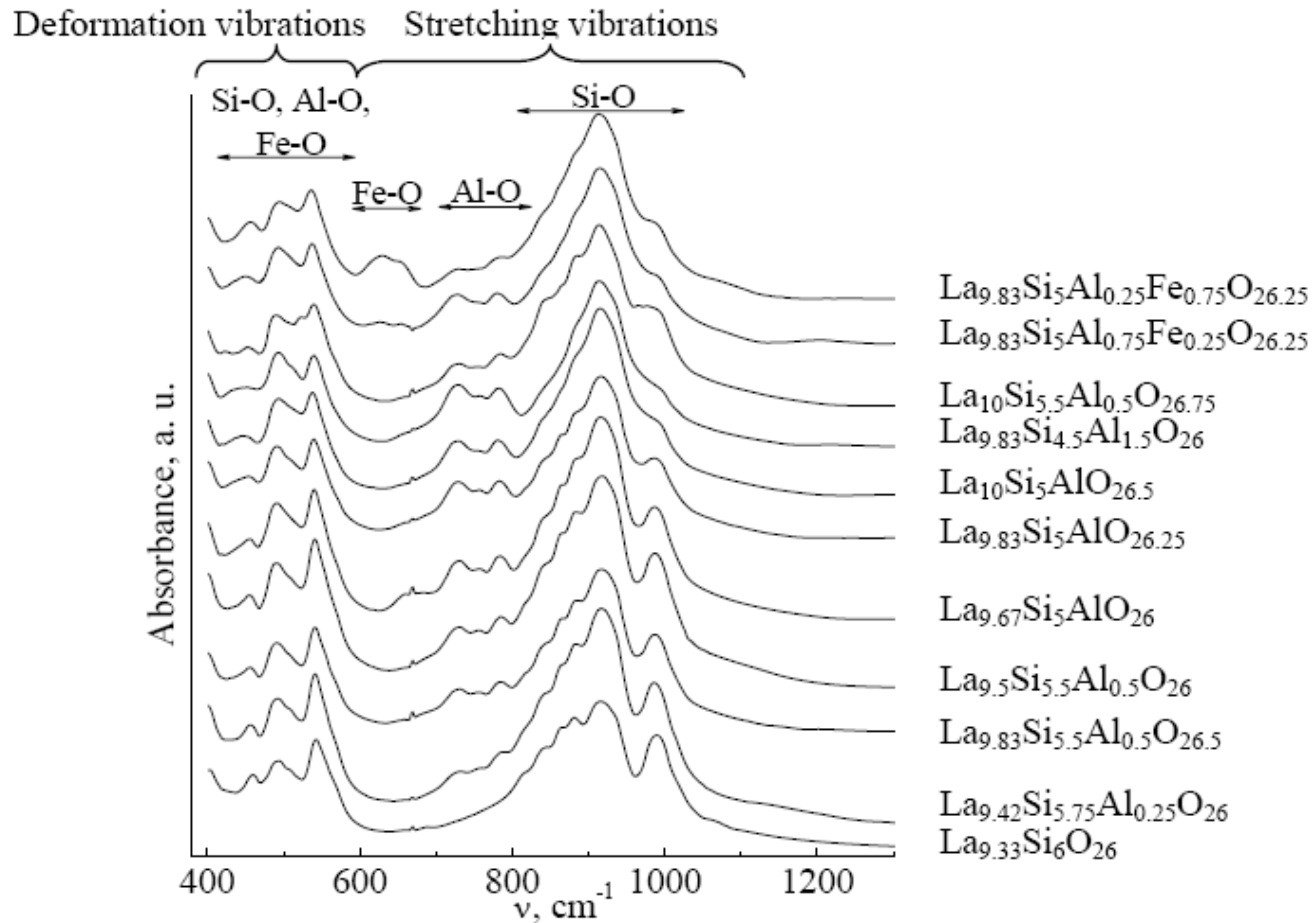
Splitting of Si-O stretching vibrations due to condensation of SiO$_4$ groups

FTIRS of lattice modes

ZrO$_2$ from hydroxide

CeO$_2$ (1) and Ce$_{1-x}$Sm$_x$, at x=0.05 (2), 0.1 (3), 0.15 (4) and 0.2 (5).

Strongly asymmetric oxygen coordination sphere in m-ZrO$_2$ (7-fold).
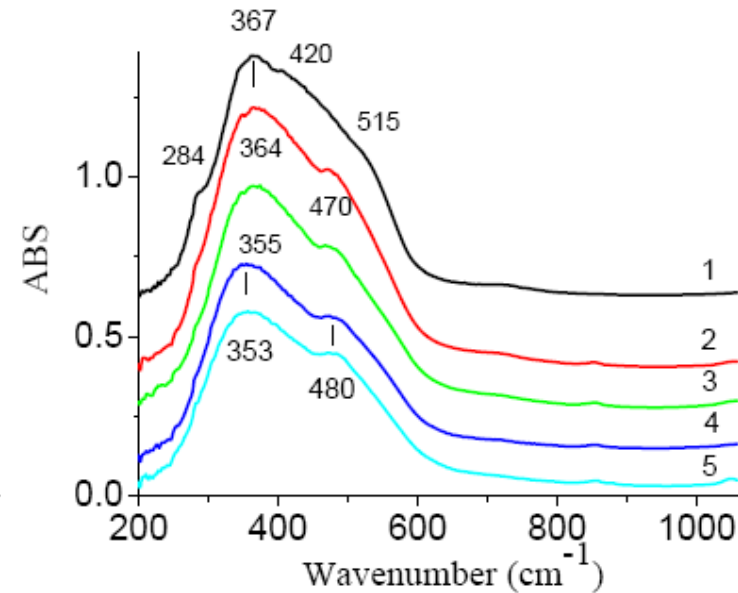
Increase of Ce-O coordination sphere deformation with doping

Raman (combined scattering of photons)
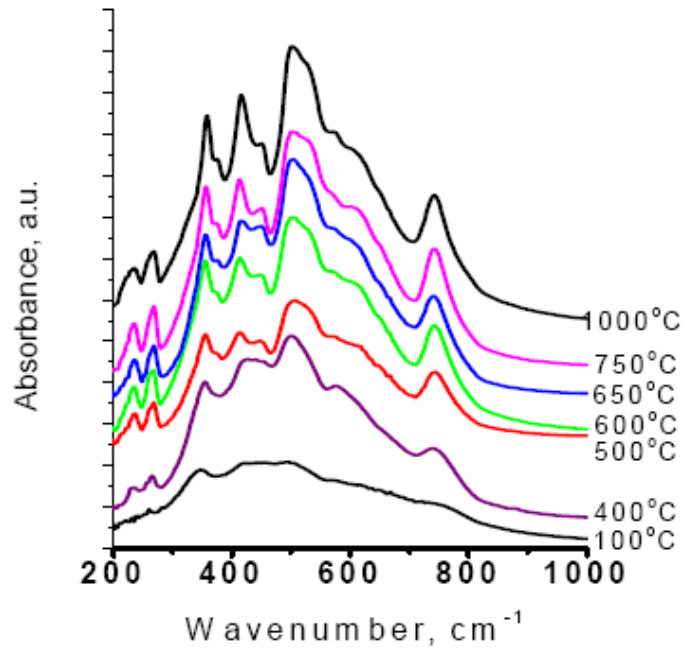

(a)
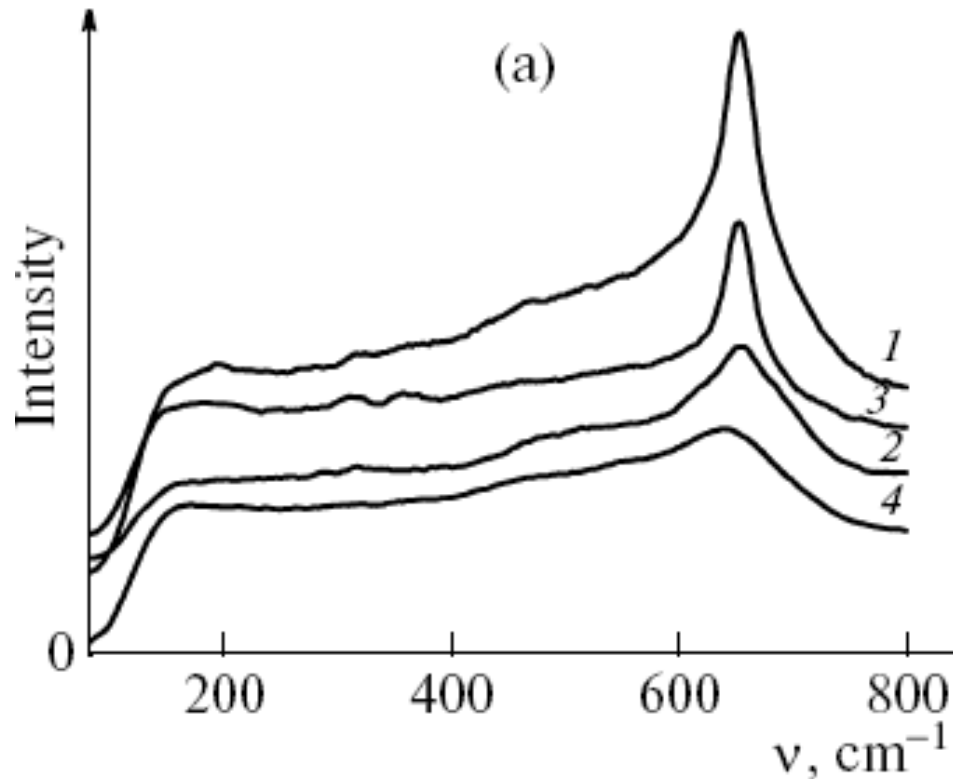
Exitation by 514.5 nm line of Ar^+ laser
(*1*) LaCeMn, (*2*) LaFeMn, (*3*) LaBiMn, and (*4*) LaSrBiMn calcined at 500°C,

Number and intensity of lines is determined by local lattice symmetry affected by the presence of defects and nanostructuring

Band at ~ 650 cm^{-1} is due to presence of nanofragments with the structure of layered perovskites in low-temperature manganites

Raman

ZrO$_2$

400°
500°
600°
650°
700°
1000°

Intensity, a.u.

Wavenumber, cm^{-1}
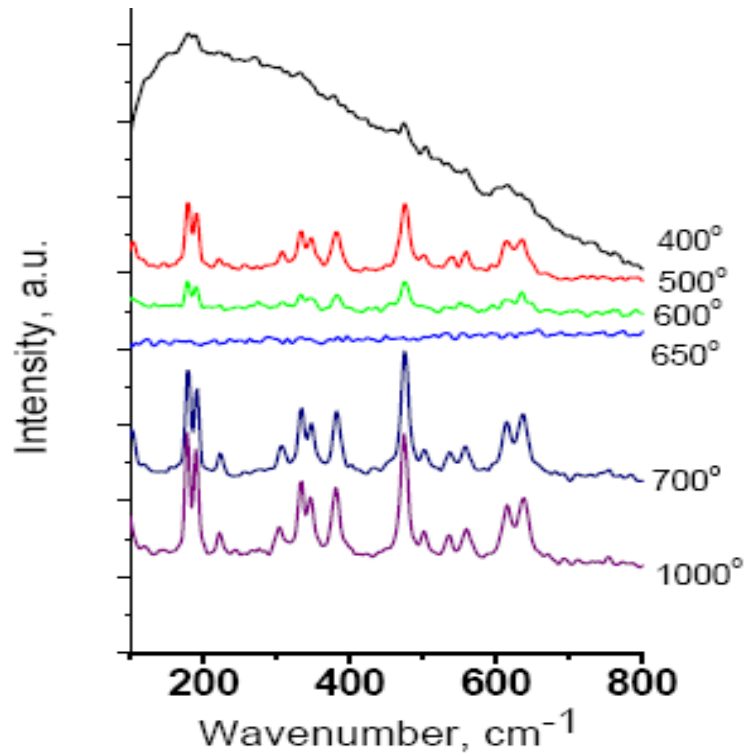
Disappearance of Raman bands for samples with multiply twinned structure

CeO$_2$ (1) and Ce$_{1-x}$Sm$_x$, at x=0.05 (2), 0.1 (3), 0.2 (4) and 0.4 (5).

463

Intensity (a.u.)

Raman shift (cm^{-1})
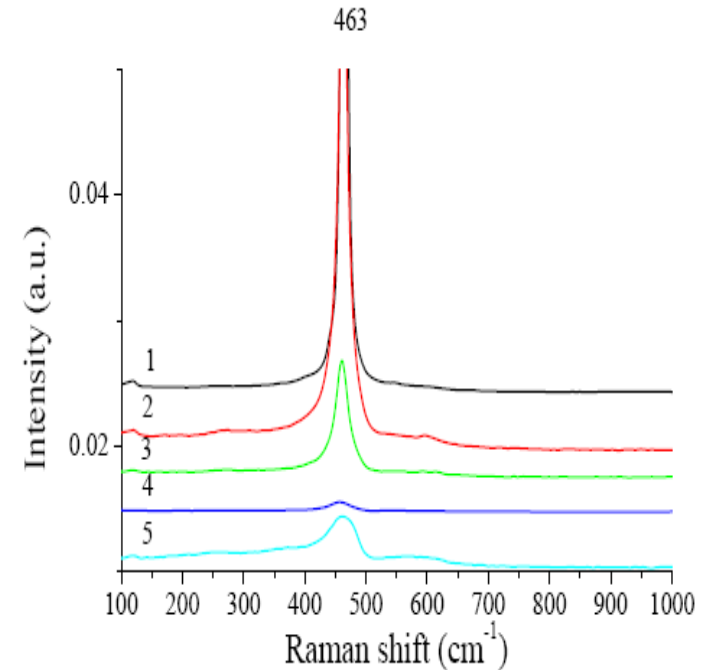
Decrease of Raman band intensity due to disordering up to x=0.2. Splitting bands at x=0.4 due to local structure rearrangement.

Raman
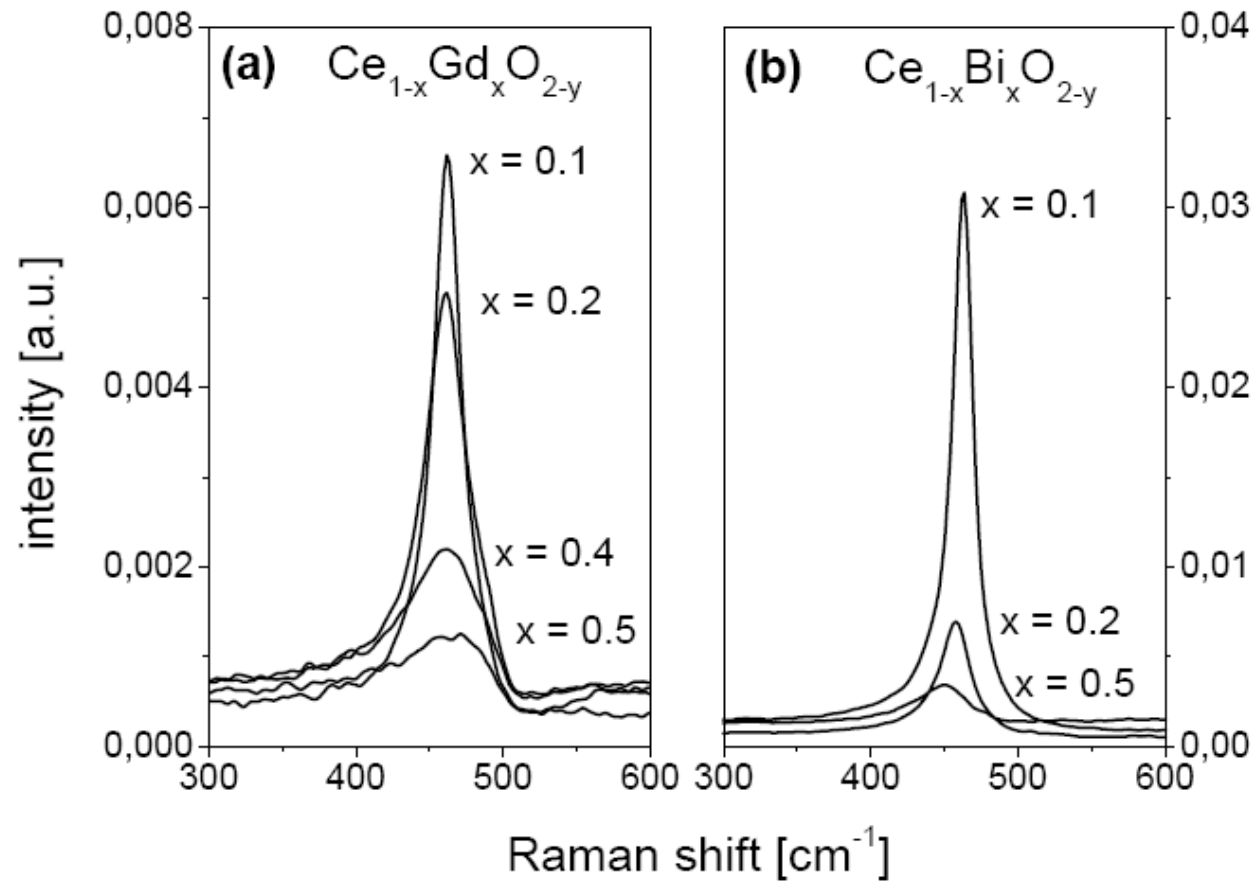
Disordering with doping as well

Mossbauer spectroscopy
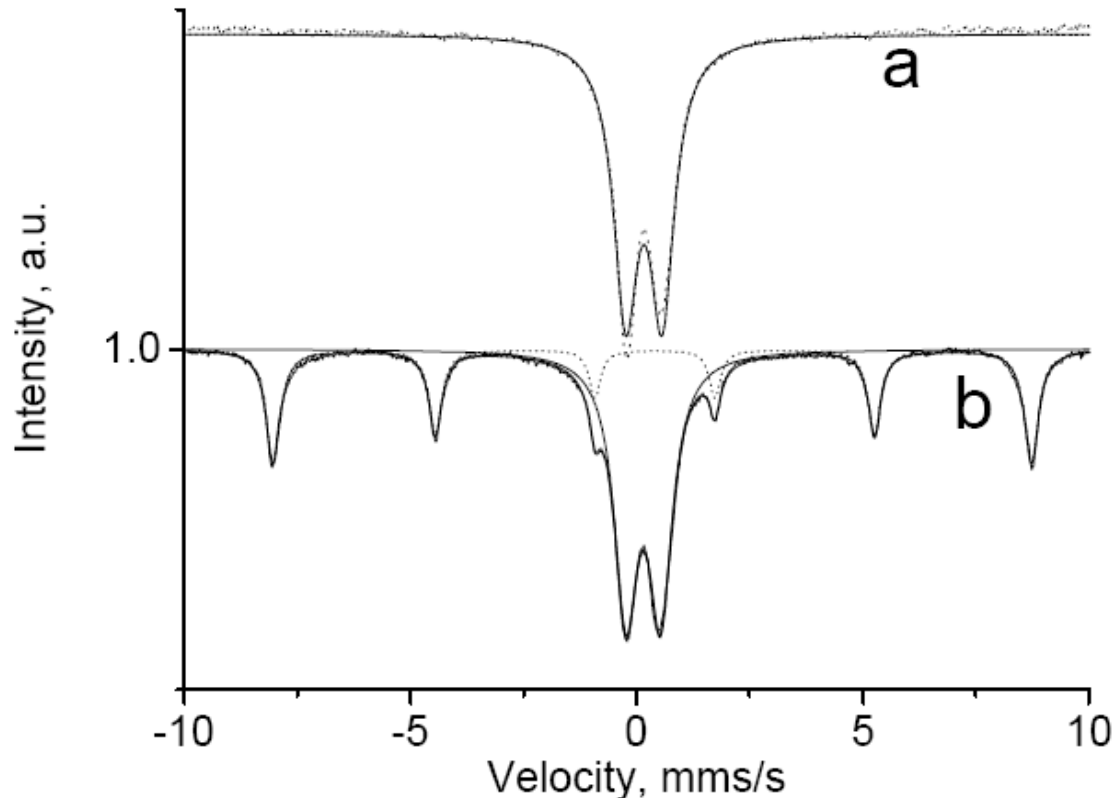
^{57}Fe absorbs γ-quantum emitted by Co isotope in a source.
Absorption resonance depends upon matching initial and final states sensitive to charge, coordination and magnetic state of Fe nuclei in a target

$La_{9.83}Si_{5.5}Fe_{0.5}O_{26.5}$(a) and $La_{10}Si_4Fe_2O_{26}$ (b).

Symmetrical doublet – isolated Fe^{3+} cations in distorted Td
Sextet - magnetically coupled Fe^{3+} cations in Oh ($LaFeO_3$)

Mössbauer spectroscopy

LSNF 1200 °C
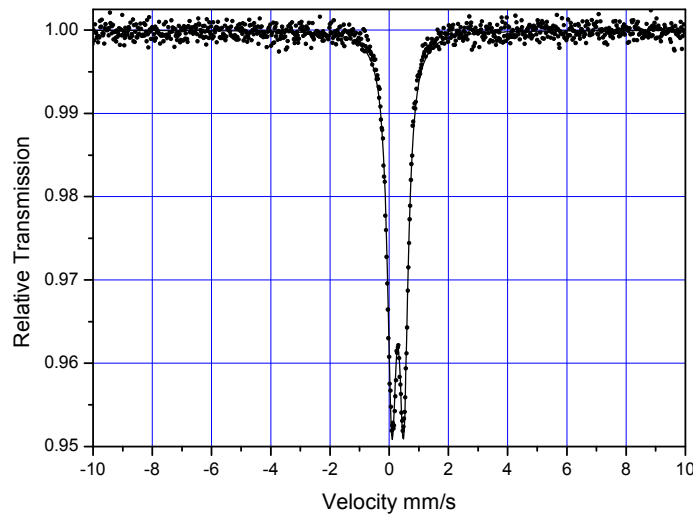
LSNF+GDC 1200 °C

Doublet due to Fe dilution by Ni
Chem. shift 0.29(1) mm/s
Quadr. splitt. QS 0.40(1) mm/s
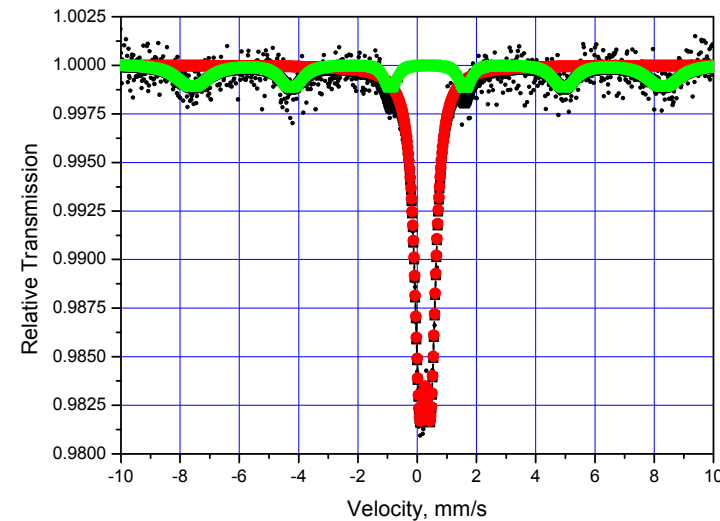
30% sextet :

H_{eff} 495 kOe, chem. shift 0.36, QS 0.00
 70% doublet , chem. shift 0.27,QS 0.37

Local depletion of perovskite phase in nanocomposite by Ni due
 to its segregation as NiO or incorporation into GDC surface layers

Mössbauer spectroscopy

La$_{1-x}$Sr$_x$FeO$_{3-y}$ perovskites with x=0.3 (left) and x=0.8 (right)

Singlet is due to Fe^{4+} state

Mössbauer spectroscopy

La$_{1-x}$Sr$_x$FeO$_{3-y}$ system

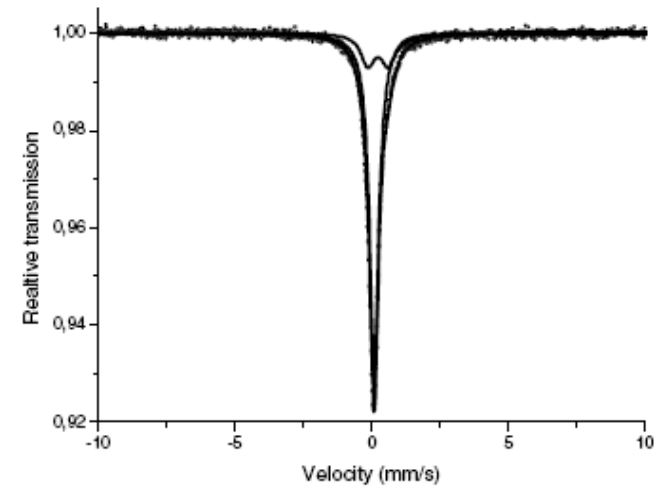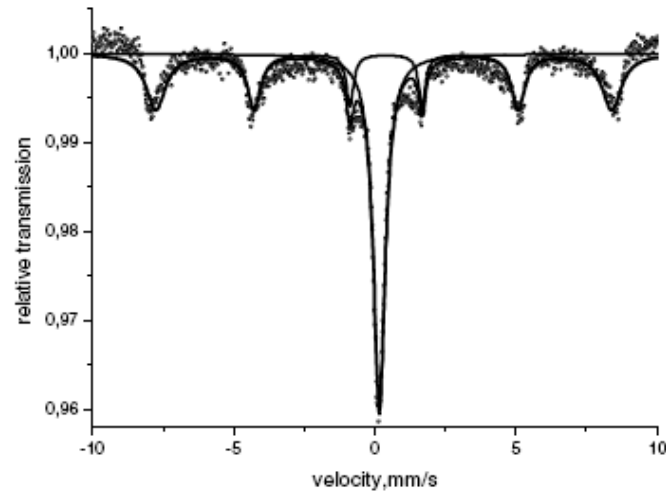| Components		O1 $\delta=0.37-0.36$		O2 $\delta=0.35$		D1 $\Delta\sim0.3$	D2 $\Delta=0.15$	S	
Sample	S$_{sp.}$	H$_{eff}$	I, %	H$_{eff}$	I, %	I, %	I, %	δ	I, %
LaFeO$_{3-y}$	1.4	522	100						
La$_{0.8}$Sr$_{0.2}$FeO$_{3-y}$	3.1	511	27	425	66			0.17	7
La$_{0.7}$Sr$_{0.3}$FeO$_{3-y}$	2.6	503	51					0.16	49
La$_{0.4}$Sr$_{0.6}$FeO$_{3-y}$	1.3							0.14	100
La$_{0.2}$Sr$_{0.8}$FeO$_{3-y}$	0.9					21		0.09	79
SrFeO$_{3-y}$	0.1					9	44	0.03	47

Variation of coordination and charge state of Fe with composition

Secondary Ions Mass Spectrometry (SIMS)

Surface layer is sputtered by ion beam (Ar^+), and emitted ion currents are analyzed by MS
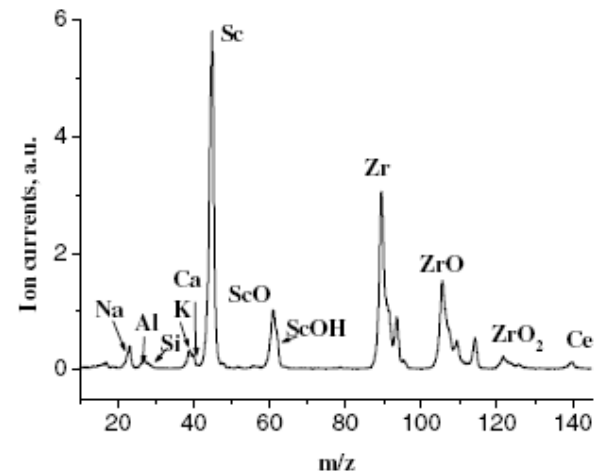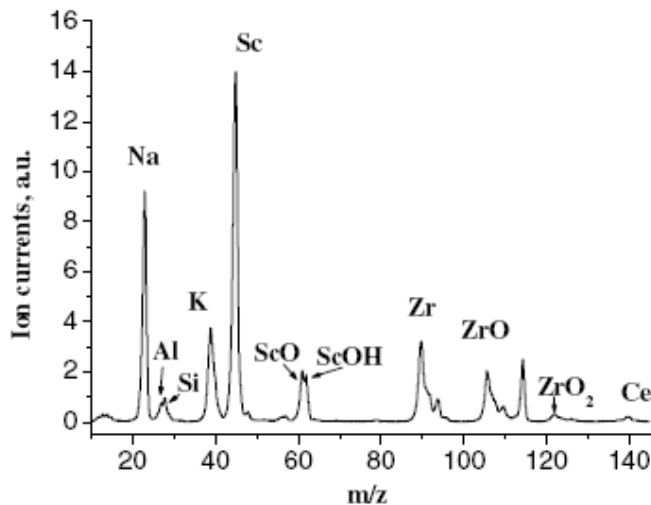
Typical mass-spectra for the surface layer (left) and the bulk (right) of ScCeSZ (Praxair) sample

+ admixed cations, + MeO^+ ions etc

SIMS
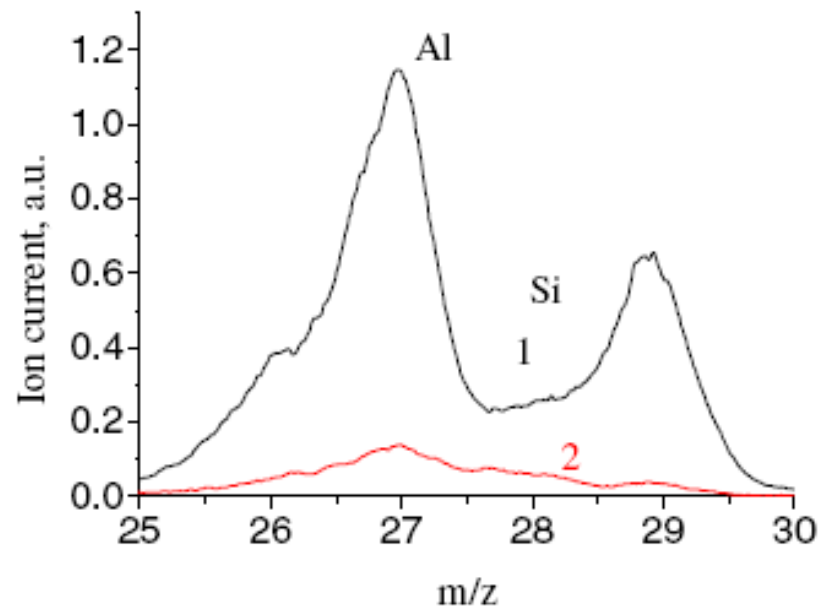
Comparison of the Al and
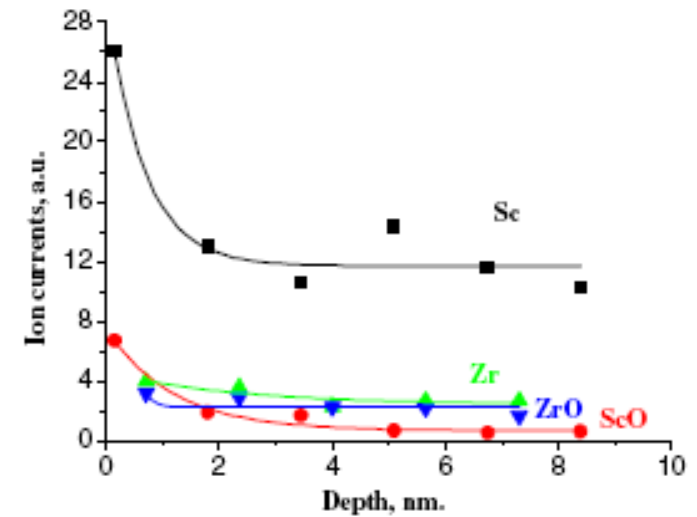Si content in the bulk (1) and in the
surface layer (2) of ScCeSZ (DKKK)
sample

Surface is contaminated by admixed cations

Variation of the ion currents
with sputtering depth for DKKK
sample

SIMS

SIMS ratio of ion currents for doped ceria-zirconia samples

Sample	Zr^+/Ce^+		$(La,Gd)^+/Ce^+$	
	Surface*	Bulk**	Surface*	Bulk**
$Ce_{0.5}Zr_{0.5}O_{2-y}$	0.12	0.11	-	-
$Ce_{0.4}Zr_{0.4}La_{0.2}$	0.15	0.25	0.55	0.55
$Ce_{0.35}Zr_{0.35}La_{0.3}$	0.20	0.35	0.9	0.9
$Ce_{0.4}Zr_{0.4}Gd_{0.2}$	0.25	0.30	0.08	0.08
$Ce_{0.35}Zr_{0.35}Gd_{0.3}$	0.15	0.25	0.10	0.10

* Within depth of 0.5-1 nm; **-after sputtering ~5-10 nm.

Surface is depleted by small Zr cations

SIMS
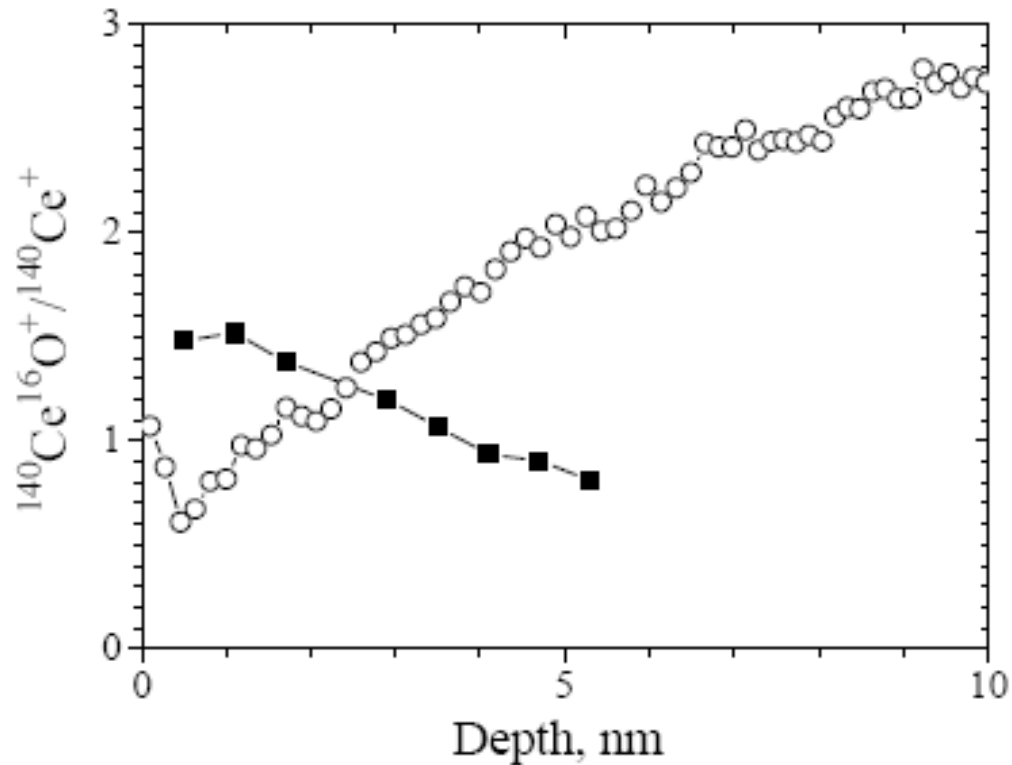
Ratio of ion currents CeO+/Ce+ versus sputtering depth for ceria-zirconia samples doped with 20 % La (circles) or Gd (squares).

Average strength of Ce-O bond proportional to CeO$^+$/Ce$^+$ ion current ratio strongly varies with the type of dopant and distance from the surface

Secondary Ions Mass Spectrometry (SIMS)
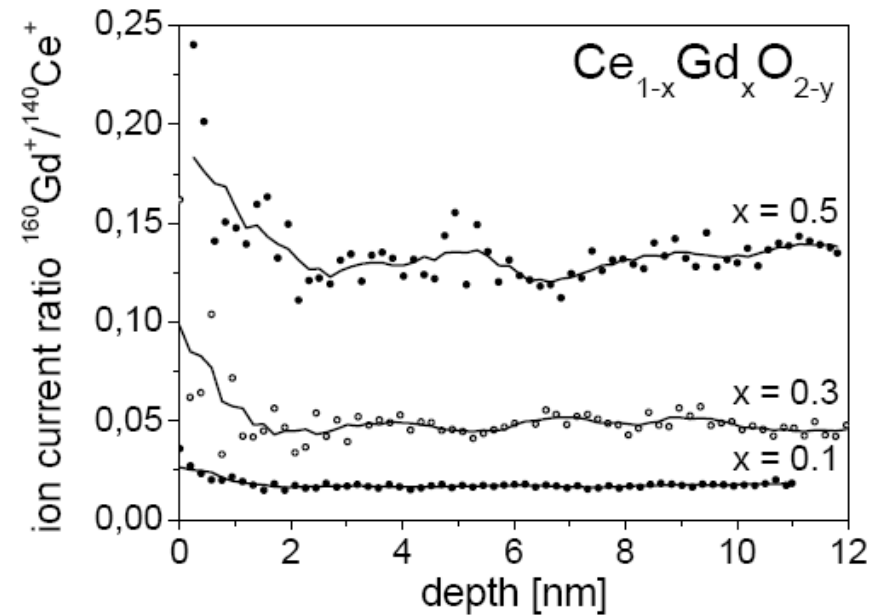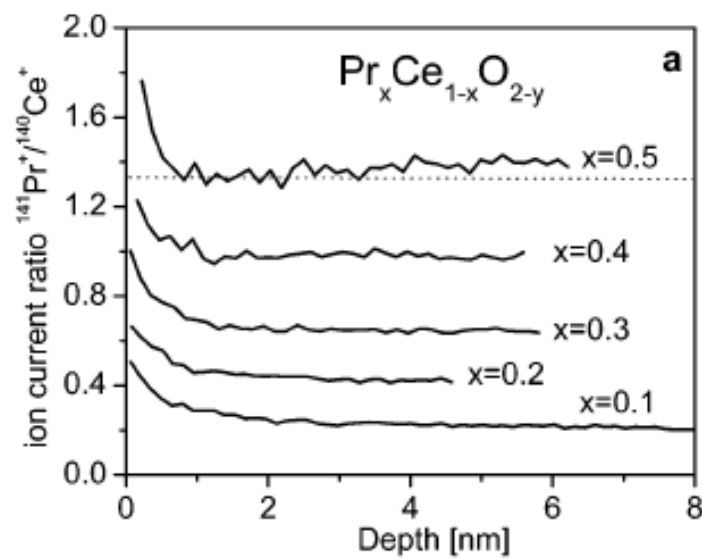
Enrichment of doped ceria surface layers by dopants

SIMS
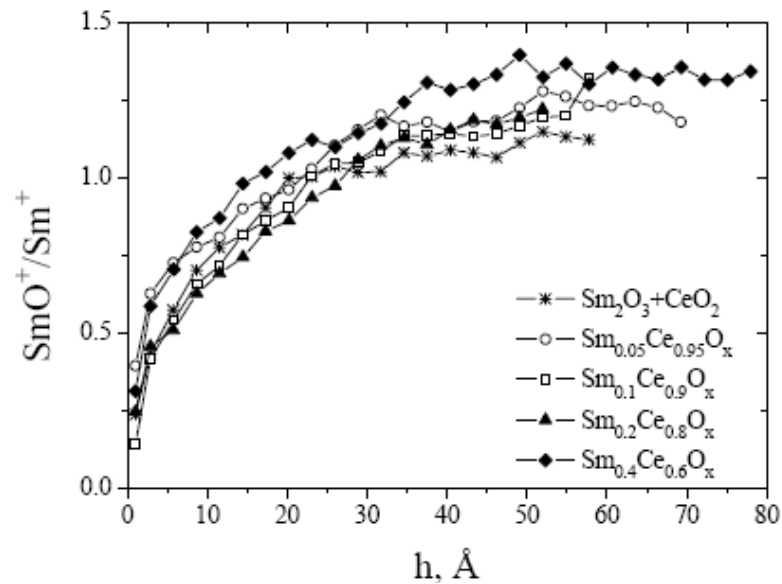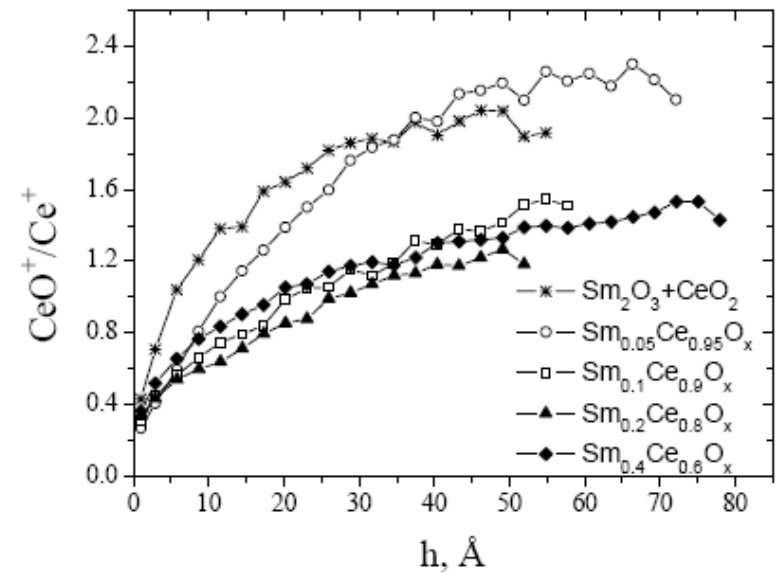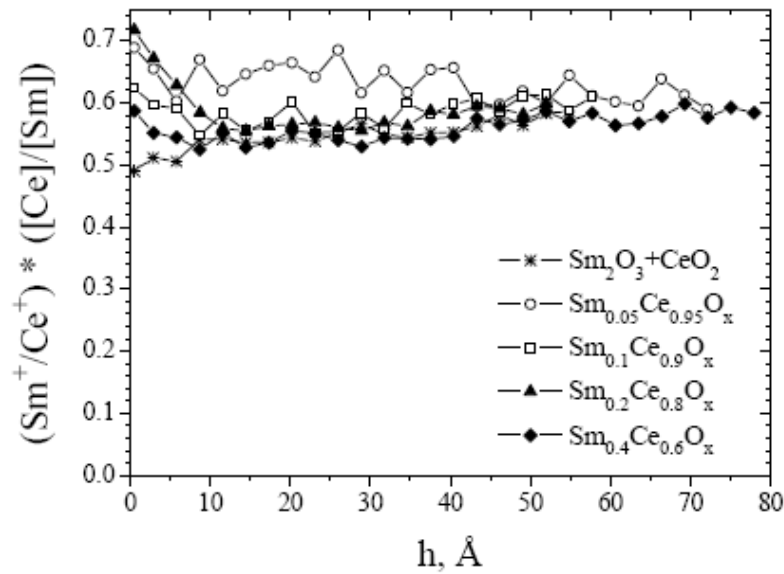
Decreased Me-O bonding strength in disordered surface layer of Sm-doped ceria ⇒enhanced surface ion conductivity

X-ray Photoelectron Spectroscopy

- <u>Principle:</u> X-ray photon emits electron from different energetic levels of surface atoms, kinetic energy of electrons determined by detector allows to estimate binding energy of a given energy level (function of charge state and coordination sphere), their intensity –surface concentration of elements within probing depth.

Surface composition by XPS for Sr-doped perovskites

$La_{0.8}Sr_{0.2}Fe_{0.6}Ni_{0.4}O_3$
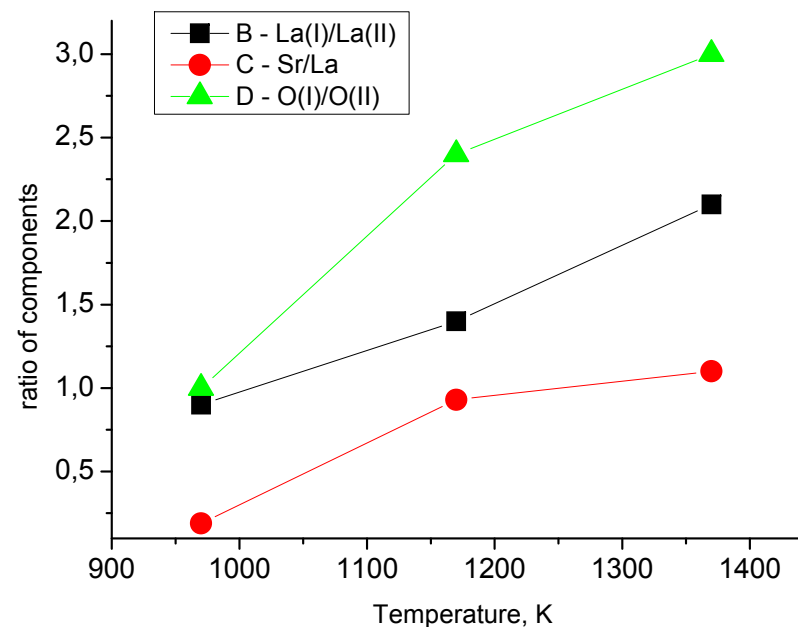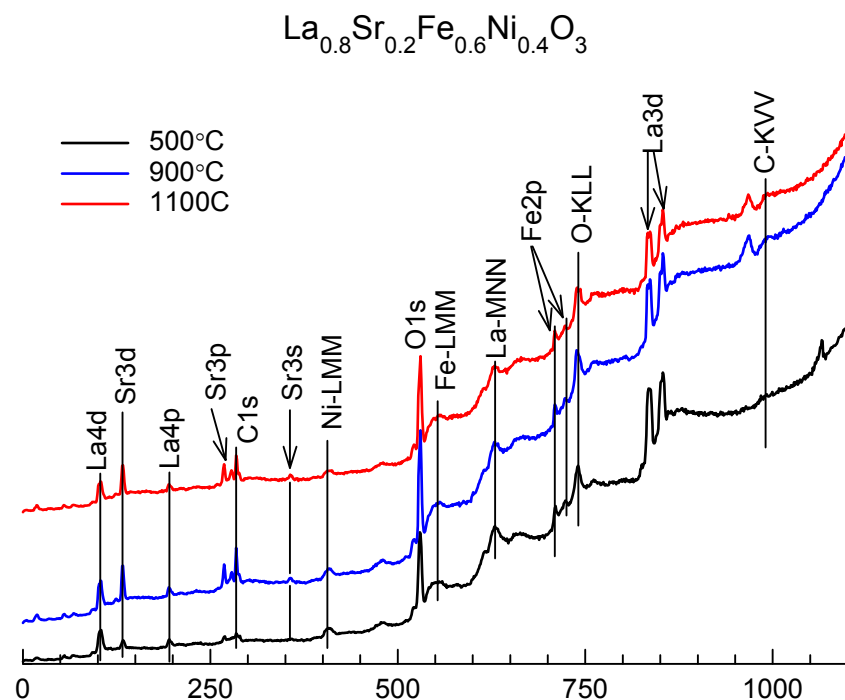
Plenty of carbonates in the surface layer, progressive Sr segregation on the surface with ↑annealing T, two forms of oxygen –ionic and covalent, + two states of La differing by BE/effective charge. ⇒ modification of surface layer due to segregated Sr, could result in degradation at IT range

XPS: nanocomposites

XPS spectra of La and Sr cations in the surface layer of LSM-ScCeSZ nanocomposites sintered at different temperatures
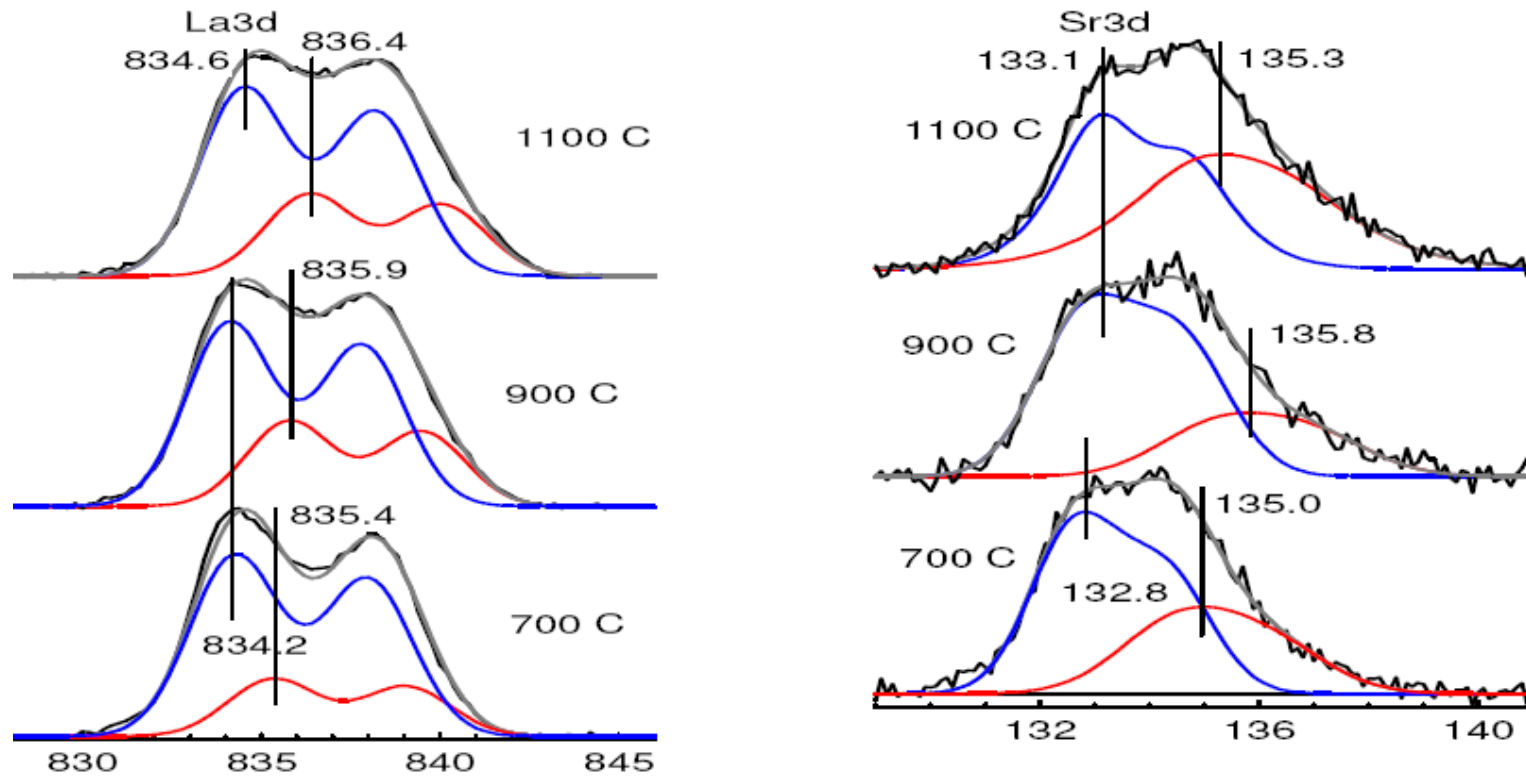
Two states of cations redistributed between P and F phases

XPS
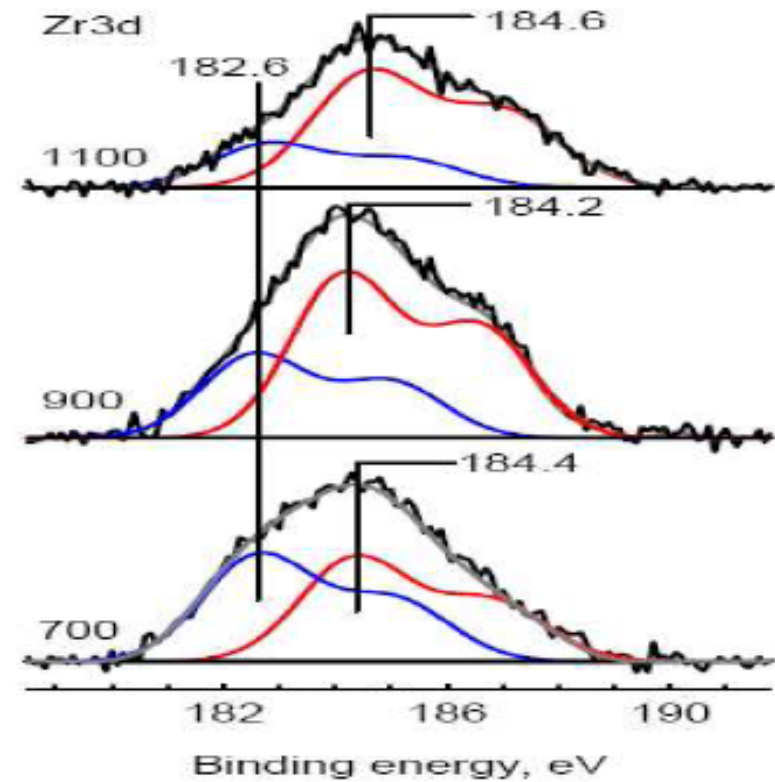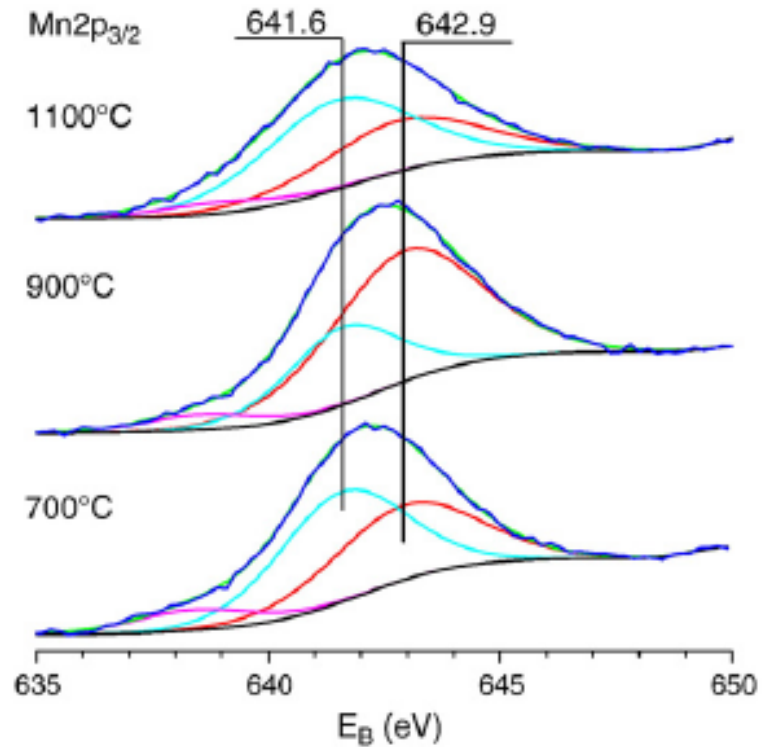
Two types of Zr and Mn cations differing by local coordination numbers and effective charge

XPS: surface composition
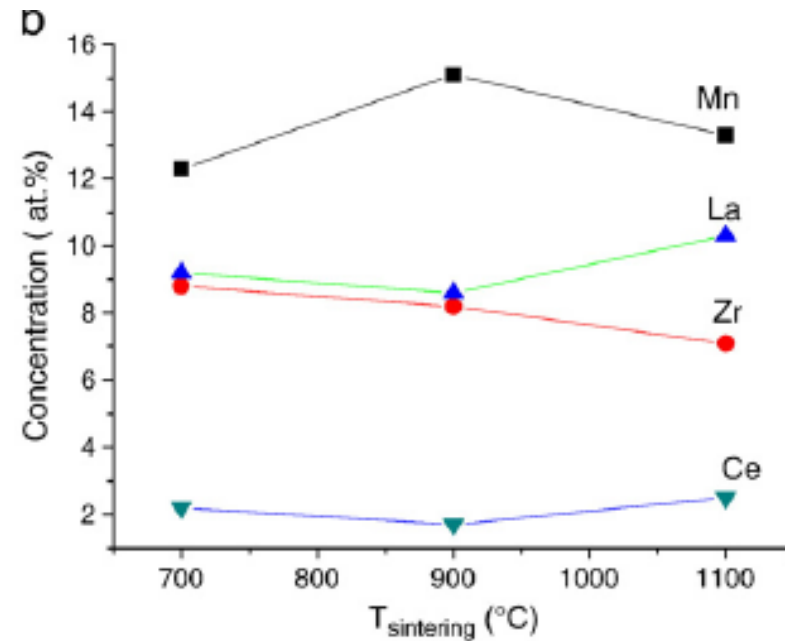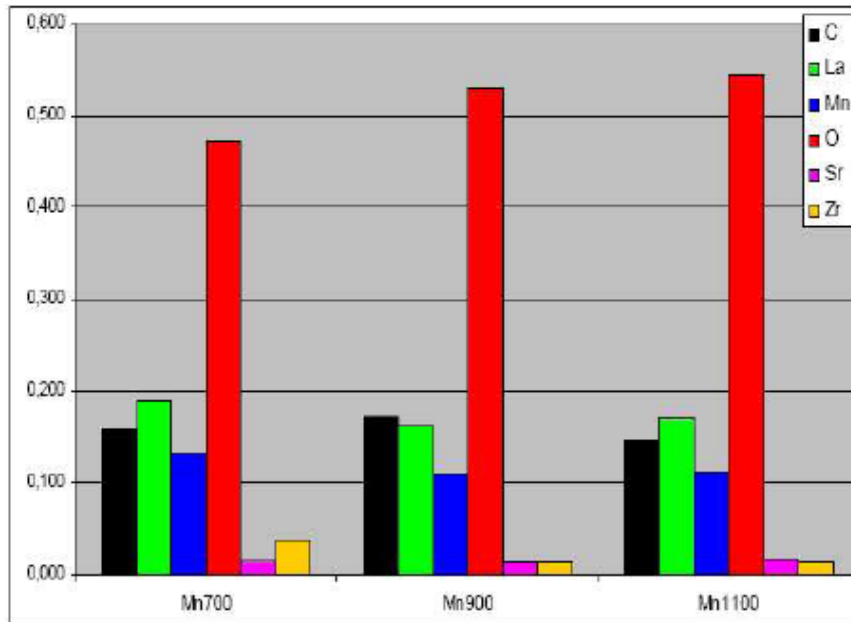
Carbon is present on the surface (carbonates)
Mn and La are transferred onto ScCeSZ surface

XPS: surface segregation
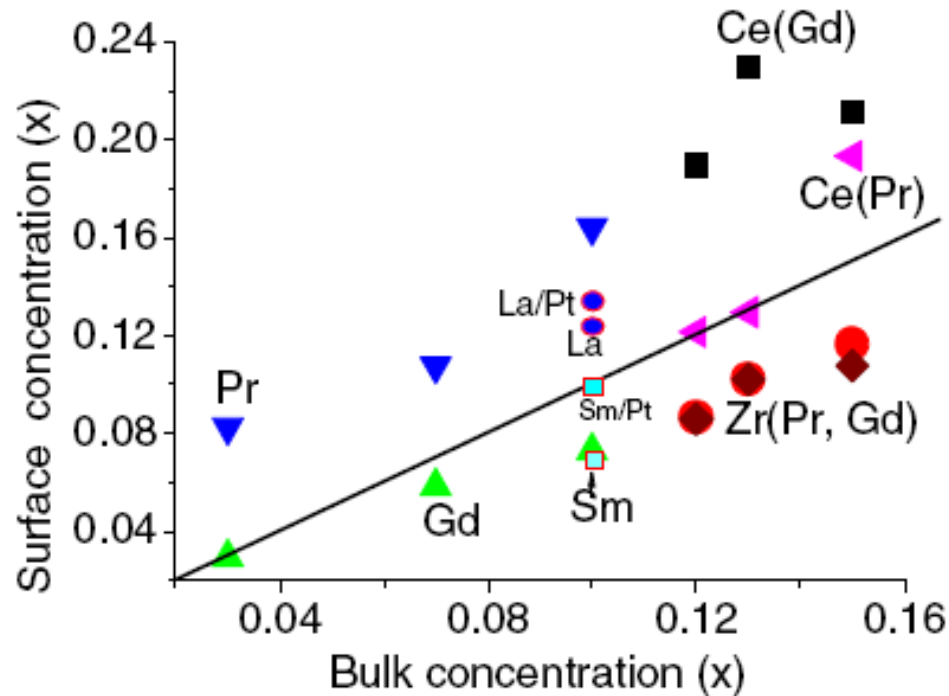
Surface (XPS) vs bulk composition for doped ceria – zirconia samples (type of doping cation indicated in parenthesis). La/Pt (Sm/Pt) - samples with supported Pt (1.4wt.%).

Segregation of big cations in the surface layer

Oxygen bonding strength by calorimetry
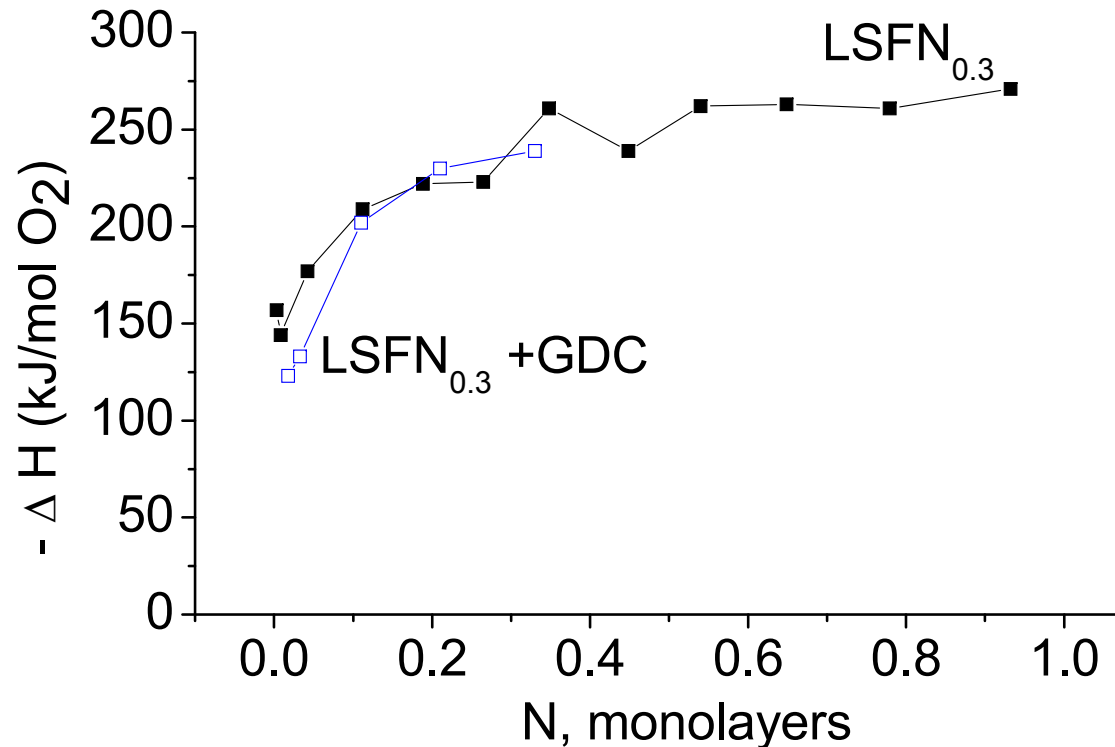
Heat of oxygen adsorption vs. amount of desorbed O_2 for $LSFN_{0.3}$ and $LSFN_{0.3}$ + GDC composite sintered at 1200 ^oC and pretreated in He at 750^0C. Pulses of O_2 in He at 450 ^oC.

Broad variation of adsorption heats, hence, oxygen bonding strength

Transport properties: Tracer diffusion coefficient of oxide ions by SIMS
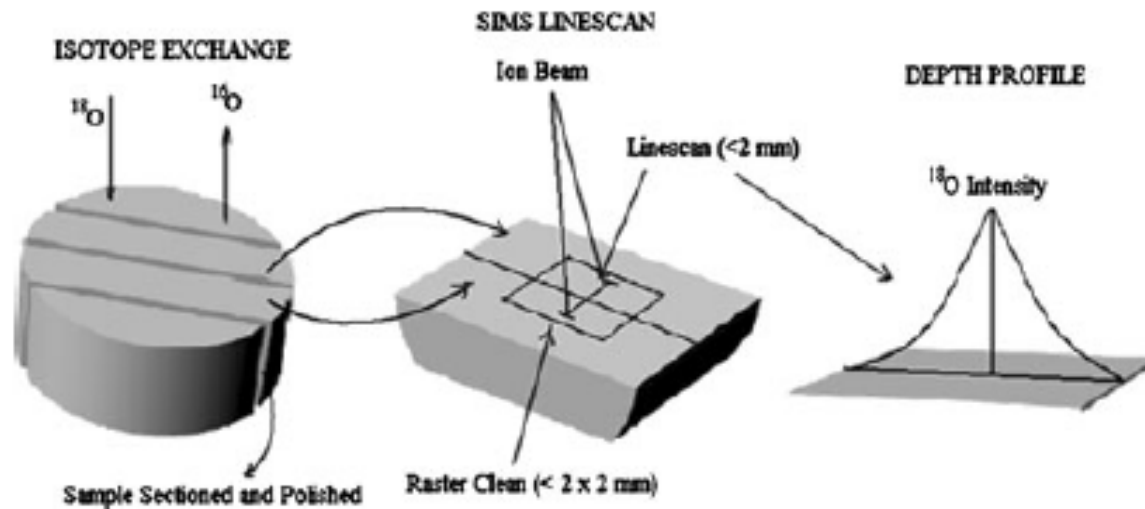
Sample is exchanged with $^{18}O_2$, then surface layer is sputtered by ion beam and ^{18}O depth profile is analyzed

$$C'(x,t) = \frac{C(x,t) - C_{bg}}{C_g - C_{bg}} = erfc\left[\frac{x}{2\sqrt{D^*t}}\right] - \left[\exp\left(\frac{kx}{D^*} + \frac{k^2t}{D^*}\right) \times erfc\left(\frac{x}{2\sqrt{D^*t}} + k\sqrt{\frac{t}{D^*}}\right)\right]$$

D^*-oxygen self-diffusion coefficient, k- surface exchange coefficient

$$k(c_g - c_s) = -D\frac{\partial C(x)}{\partial x}\bigg|_{x=0}$$

characterizing the rate of surface exchange reaction

Scale of D and k variation

La –Sr- Mn- Co- O perovskites

Broad variation controlled by defect structure, oxygen bonding strength and mechanism of oxygen migration

Diffusion parameters by weight and conductivity relaxations at pO$_2$ change –dense ceramics

$$\frac{\partial C}{\partial t} = \frac{1}{r}\frac{\partial}{\partial r}\left(D_{\text{chem}}\frac{\partial C}{\partial r}\right) \text{ for } r \text{ direction}$$

$$-D_{\text{chem}}\frac{\partial C}{\partial r}\bigg|_{r=\pm a} = k_{\text{chem}}(C - C_\infty),$$

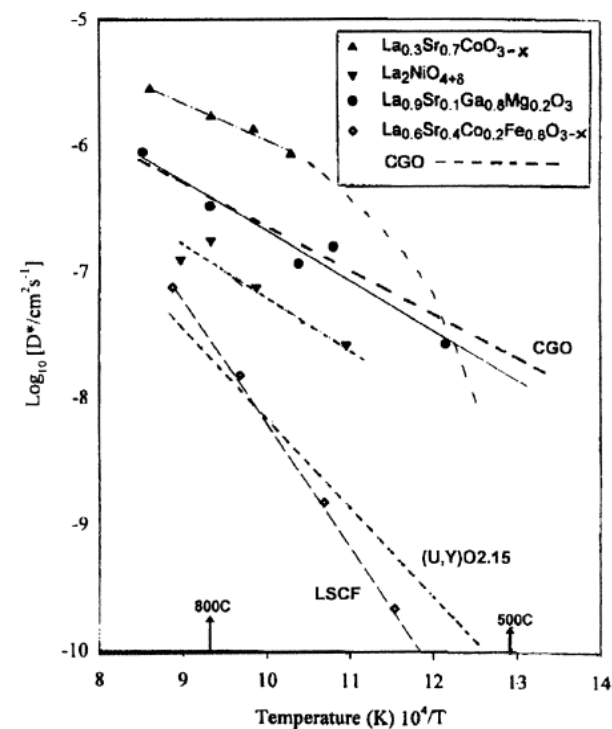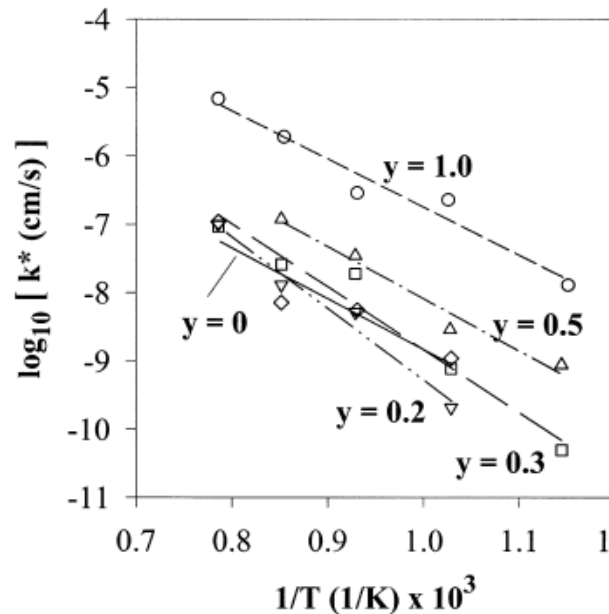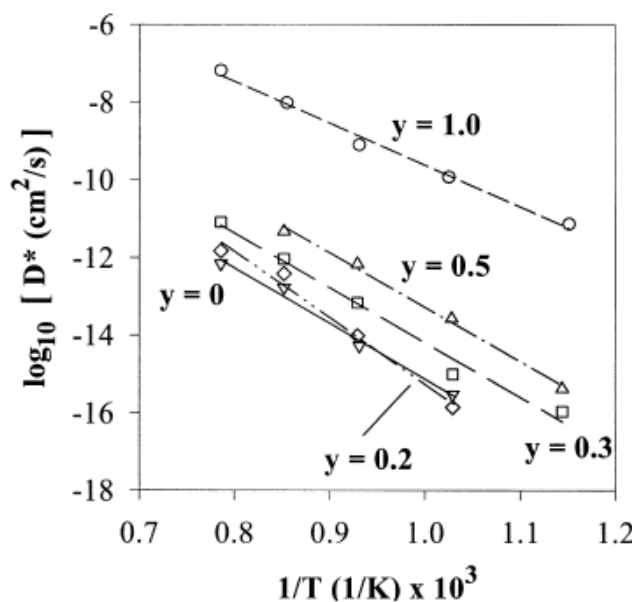$$\frac{\partial C}{\partial t} = \frac{\partial}{\partial y}\left(D_{\text{chem}}\frac{\partial C}{\partial y}\right) \text{ for length direction}$$

$$-D_{\text{chem}}\frac{\partial C}{\partial y}\bigg|_{y=\pm l} = k_{\text{chem}}(C - C_\infty)$$

$$\frac{M(t)}{M(\infty)} = 1 - \sum_{n=1}^{\infty}\sum_{m=1}^{\infty}\frac{4L_c^2\exp(-\beta_n D_{\text{chem}}t/a^2)}{\beta_n^2(\beta_n^2 + L_c^2)}$$

$$\times \frac{2L_p^2\exp(-\gamma_m^2 D_{\text{chem}}t/l^2)}{\gamma_m^2(\gamma_m^2 + L_p^2 + L_p)}$$

$$\frac{\sigma_t - \sigma_0}{\sigma_\infty - \sigma_0} = 1 - \sum_{i=1}^{\infty}\sum_{m=1}^{\infty}\sum_{n=1}^{\infty}\frac{2L_1^2\exp(-\beta_i^2\tilde{D}_0 t/h^2)}{\beta_i^2(\beta_i^2 + L_1^2 + L_1)}$$

$$\frac{\sigma(t) - \sigma(0)}{\sigma(\infty) - \sigma(0)} = 1 - \sum_{n=0}^{\infty}\frac{8}{(2n+1)^2\pi^2}\exp\left[\frac{-(2n+1)^2\pi^2 D_{\text{chem}}t}{4l^2}\right]$$

$$\times \frac{2L_2^2\exp(-\gamma_m^2\tilde{D}_0 t/w^2)}{\gamma_m^2(\gamma_m^2 + L_2^2 + L_2)} \times \frac{2L_3^2\exp(-\delta_n^2\tilde{D}_0 t/l^2)}{\delta_n^2(\delta_n^2 + L_3^2 + L_3)}$$

More simple if limited by diffusion

Typical conductivity and weight relaxations

$La_{0.6}Sr_{0.4}Co_{0.8}Fe_{0.2}O_{3-\delta}$

- experiment at 800°C
- fit

0,2100 --> 0,0700 atm $D = 5 \cdot 10^{-7}$ cm^2/s

$La_{0.8}Sr_{0.2}Fe_{0.8}Ni_{0.2}O_{3-\delta}$
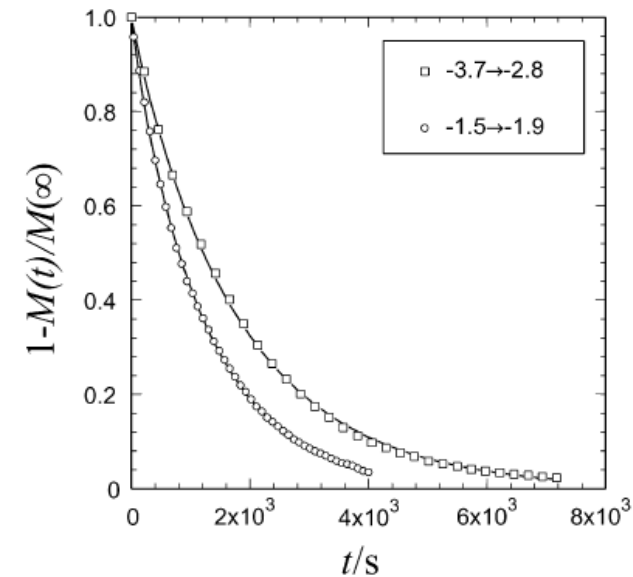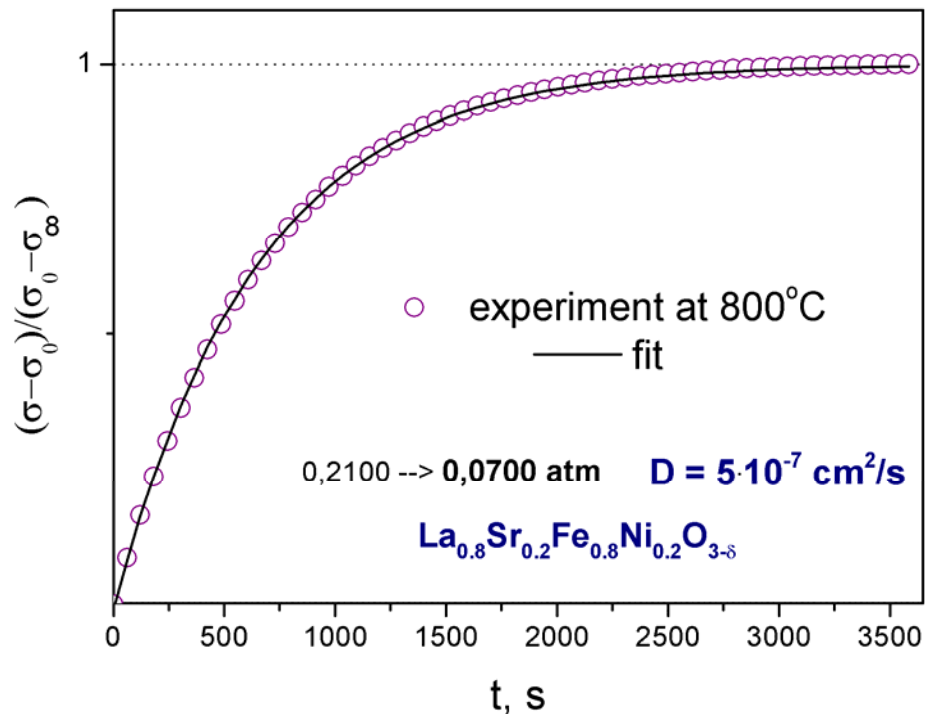
$K_{chem.} = k^*\gamma$; $D_{chem} = D^* \gamma$, where $\gamma = \frac{1}{2}\frac{\partial \ln P_{O_2}}{\partial \ln c_O}$

Can be used only for MIEC materials able to change stoichiometry, i.e. adsorb/desorb oxygen

Estimation of D_{chem}

by weight loss relaxation
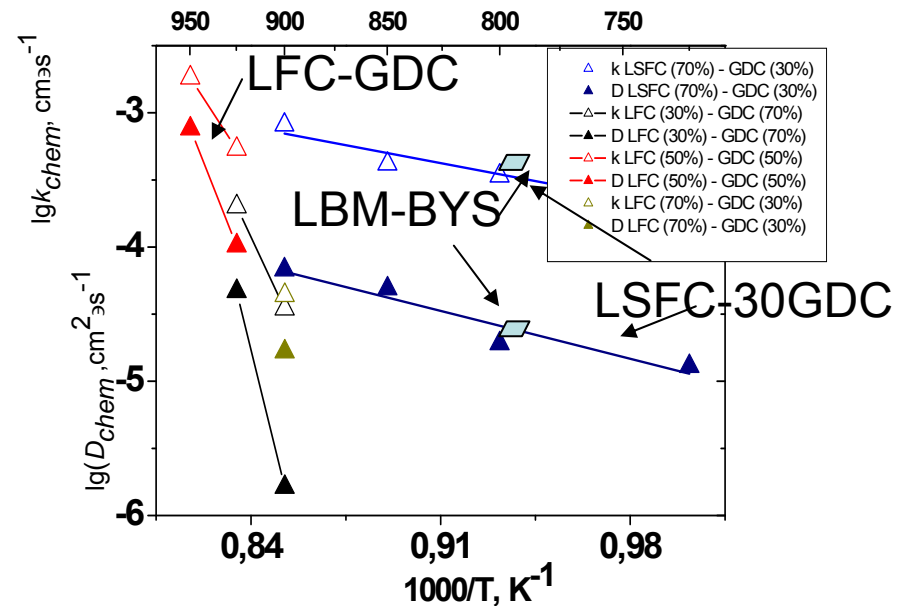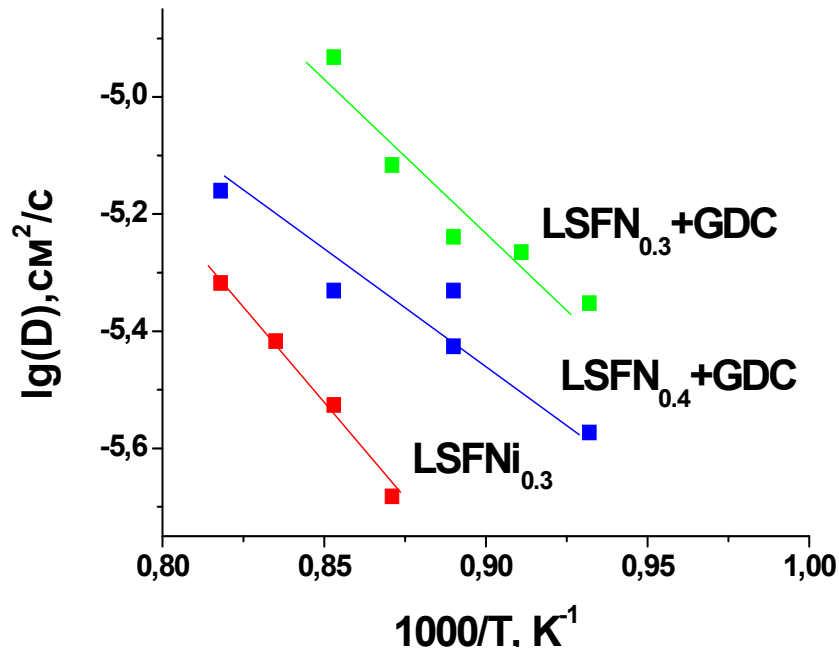
Isothermal isotope exchange in static system: typical dependencies for LSCF-30%GDC **powder**
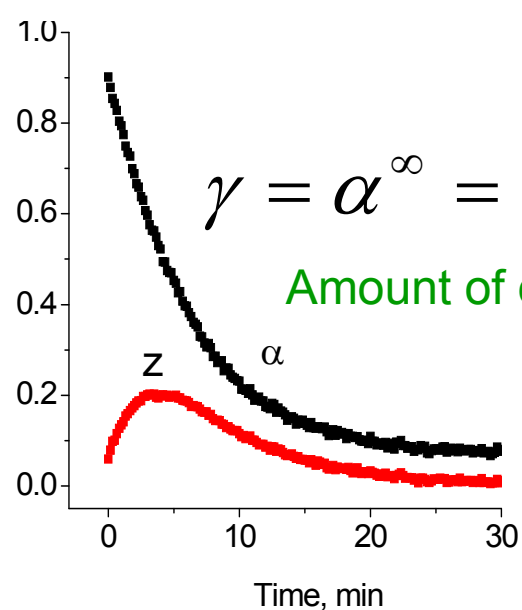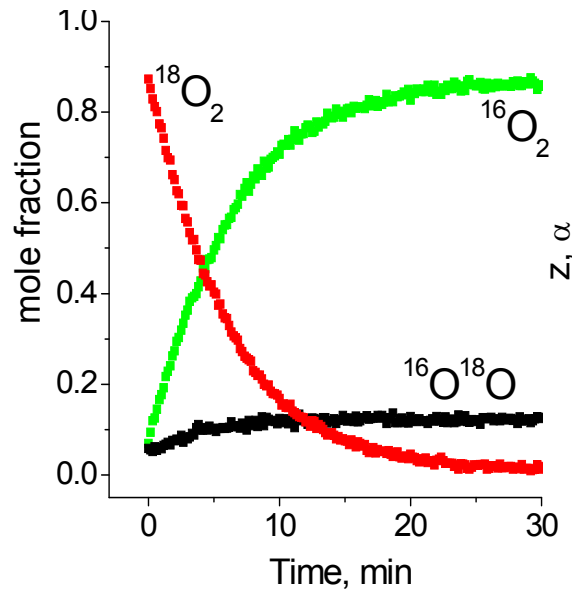
$$N_e = 2N \frac{\alpha^0 - \gamma}{\gamma}$$

$$\gamma = \alpha^\infty = \alpha_s^\infty \quad \text{equilibrium isotope fraction}$$

Amount of exchangeable oxygen > 100 ML

Dependence of $\alpha(t)$ is close to exponential $\Rightarrow$ uniform oxygen $\Rightarrow$ very fast bulk diffusion

$$Rt = -\frac{2N}{2N + N_e} \ln \frac{\gamma - \alpha}{\gamma - \alpha^0}$$

Simple estimation of R –specific rate of exchange as characteristic of surface reaction

Rate of heteroexchange ($R_o = 5.8 \ast 10^{17}$ molecules $O_2/s \ast m^2$ at 550°C and $P_{in} = 1.7$ Torr) is close to that for LSCF and is one of the highest for oxides $E_a \sim 80$ kJ/mol

Isotope exchange reactions by Muzykantov

$$^{16}O_2 + {}^{18}O_2 = 2\,{}^{16}O^{18}O \qquad \text{homoexchange}$$

$$0.5\,{}^{18}O_2 + [{}^{16}O] = 0.5\,{}^{16}O_2 + [{}^{18}O] \qquad \text{heteroexchange}$$
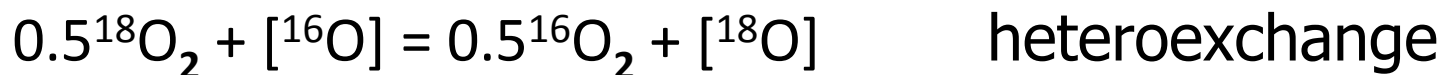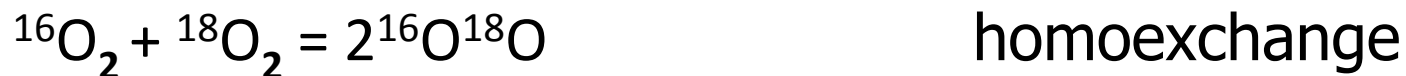
Types of exchange mechanisms

I(R^0) $\qquad {}^{16}O_2 + {}^{18}O_2 = 2\,{}^{16}O^{18}O$

II(R^1) $\qquad {}^{18}O_2 + [{}^{16}O] = {}^{16}O^{18}O + [{}^{16}O]$

III(R^2) $\qquad {}^{18}O_2 + 2[{}^{16}O] = {}^{16}O_2 + 2[{}^{18}O]$
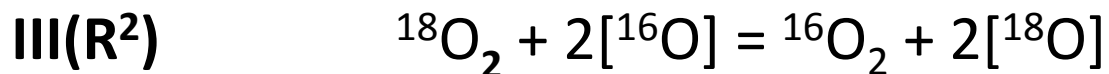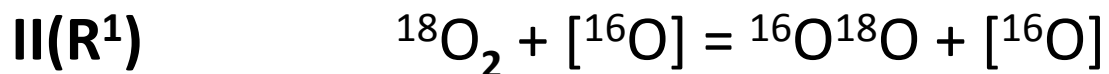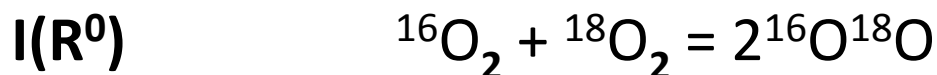
Types and Mechanisms of Dioxygen Exchange by Muzykantov

The reversible Steps of Gas–Surface–Bulk Processes realizing Exchange:

1) $O_2 + 2\,Z_{ads} \leftrightarrow 2\,ZO_{ads}$

2) $O_2 + Z_{ads} + ()_s \leftrightarrow ZO_{ads} + (O)_s$

3) $ZO_{ads} + ()_s \leftrightarrow Z_{ads} + (O)_s$

4) $(O)_s + [\ ]_v \leftrightarrow ()_s + [O]_v$

The ratio of the rates of these stages determines the shares of different types of exchange

Isotope-kinetic equations

by Muzykantov

x_0 – $^{16}O_2$ mole fraction, x_1 and x_2 – $^{16}O^{18}O$ и $^{18}O_2$, respectively

$\alpha = 0.5x_1 + x_2$ ^{18}O fraction in gas

$z = x_2 - \alpha^2$ deviation from equilibrium binomial isotope distribution

$$\frac{\partial \alpha}{\partial t} = -r(\alpha - \alpha_S)$$

$$\frac{\partial z}{\partial t} = -kz + k_3(\alpha - \alpha_S)^2$$

$r = 0.5k_2 + k_3$ Rate of heteroexchange, <time>^{-1}

$k = k_1 + k_2 + k_3$ Total rate of exchange, <time>^{-1}

Surface forms
by Muzykantov

Structure sensitivity of exchange due to variation of z_s and ( )$_s$ ratio as dependent on chemistry and defect structure

Z_{ads} – weakly bound O

( )$_s$ – strongly bound O

$$ZO_{ads} \quad (O)_s \quad Z_{ads} \quad (O)_s \quad ( )_s \quad (O)_s$$
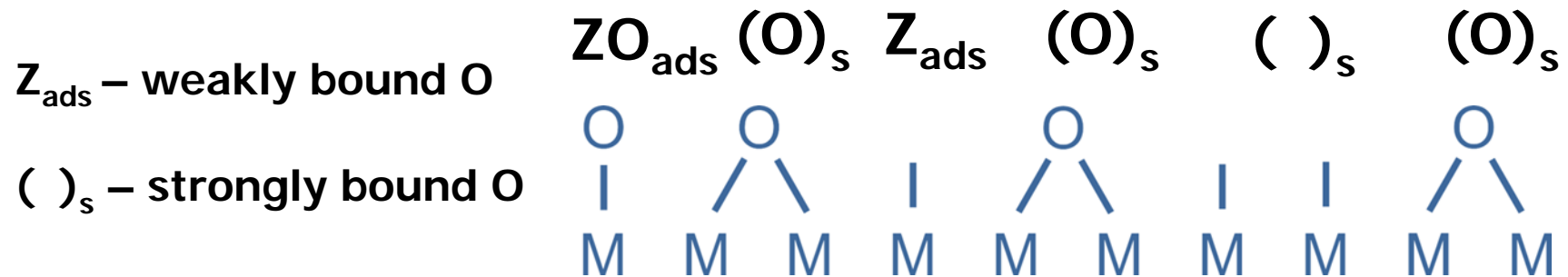
System of equations
for diffusion model of isotope exchange in closed system

$$N \frac{\partial \alpha}{\partial t} = -N_S R(\alpha - \alpha_s)$$

$$N_S \frac{\partial \alpha_s}{\partial t} = N_S R(\alpha - \alpha_s) - N_{bulk} \frac{D}{h^2} \frac{\partial \alpha_{bulk}}{\partial \eta}\bigg|_{\eta=0}$$ h-characteristic size of oxide particle

$$\frac{\partial \alpha_{Obulk}}{\partial t} = \frac{D}{h^2} \frac{\partial^2 \alpha_{Obulk}}{\partial \eta^2}$$ η-dimensionless depth of the oxide layer

$$N \frac{dx_1}{dt} = N_S R \left[(1-b)(\alpha(1-\alpha_s) + \alpha_s(1-\alpha) - x_1) + b(2\alpha_s(1-\alpha_s) - x_1) \right]$$

$$N \frac{dx_2}{dt} = N_S R \left[(1-b)(\alpha\alpha_s - x_2) + b(\alpha_s^2 - x_2) \right]$$

b- a share of the exchange mechanism III in the overall exchange rate R

Initial and boundary conditions

$$\alpha = 0.96 \qquad \eta = 0 \qquad \alpha_{bulk} = \alpha_s \qquad \alpha_{bulk} = 0 \qquad \alpha_s = 0$$

Powders vs. dense ceramics: comparison for LSFC-GDC case studies
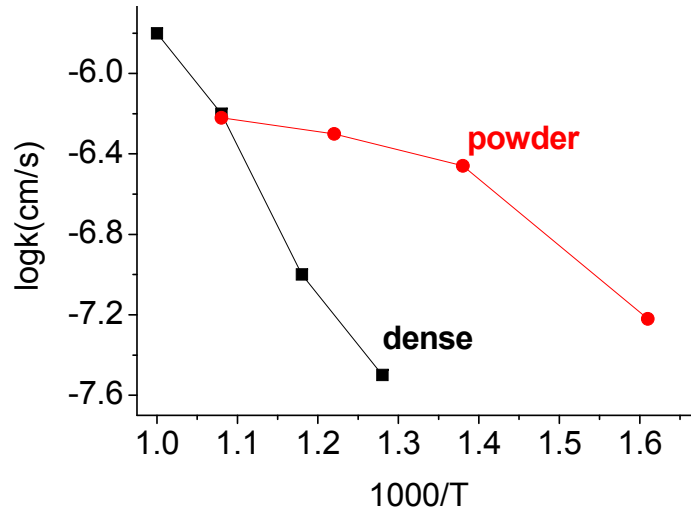
Powder-isotope exchange in static reactor; dense –SIMS IEP
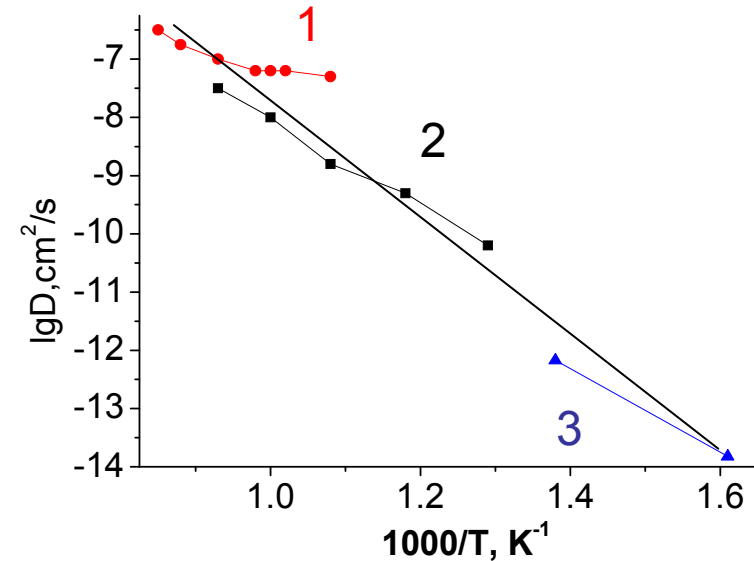
1-weight relaxation, pellet
2-SIMS IEP, pellet
3- isotope exchange, powder

Reasonable agreement in D as bulk property
Much higher sensitivity of k to surface state-defects, admixtures etc.

Scale of surface reactivity by the rate of oxygen heteroexchange

Samples sintered at 1100 ^{o}C
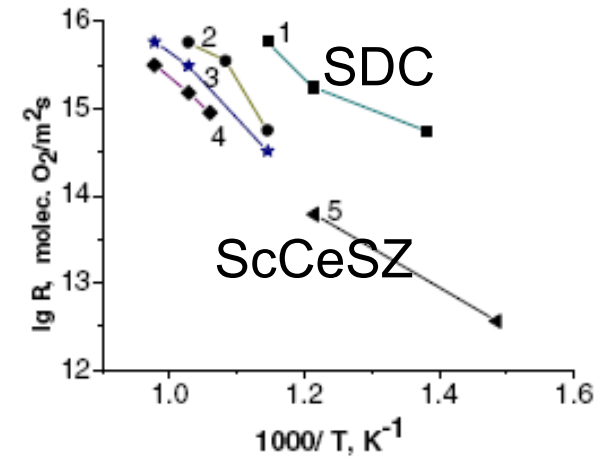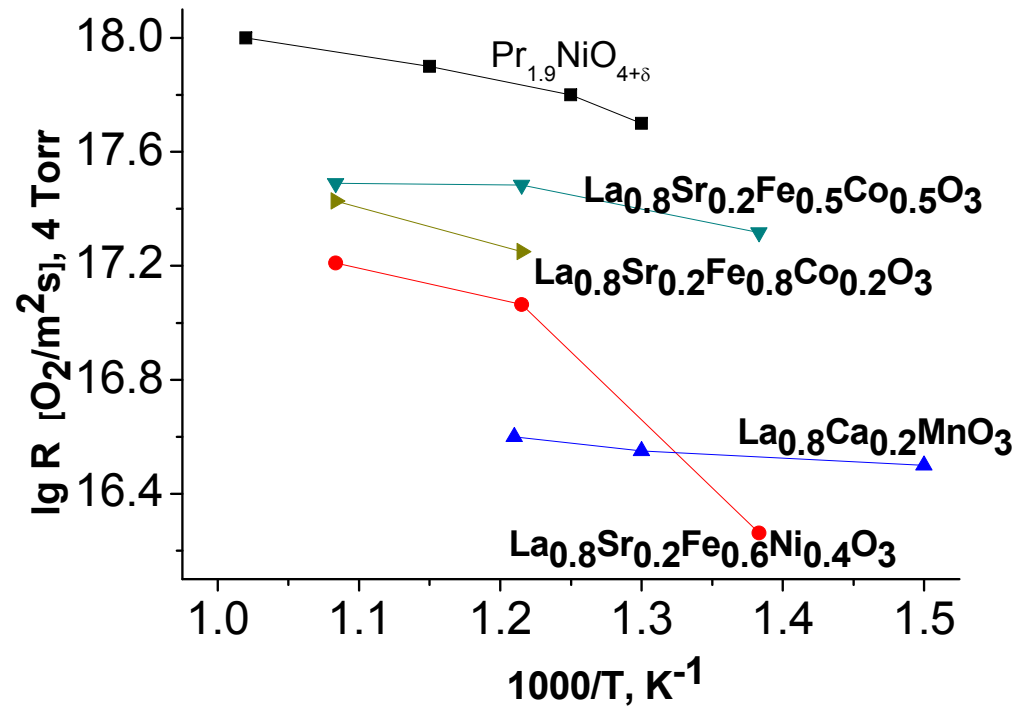
Variation of specific reactivity by two order of magnitude for perovskites
Much lower reactivity of surface sites for electrolytes, especially doped zirconia

SSITKA (powders, flow reactor)

M1 - 1 % $^{16}O_2$ in He,
M2 - 1% $^{18}O_2$ or 1% $^{18}CO_2$ in He, plug flow reactor, contact time 0.01 s, 600-800 °C

M1

exit ← ⊘ → reactor → GA-MS

M2

Pr$_2$NiO$_x$ 1100 (S=0.4 м2/г)

R=7 min^{-1}

D > 1 . 5 m i n^{-1}

mole fractions

t, s

D = 1.4 *10^{-10} cm^2/s at 600 °C

La$_{0.8}$Bi$_{0.2}$MnO$_3$

В)

R=12 min^{-1}, S = 1 3

D = 0 , 1 7 m i n^{-1} t t = 3 8

mole fractions

t, s

D= 6 *10^{-14} cm^2/s at 600 C
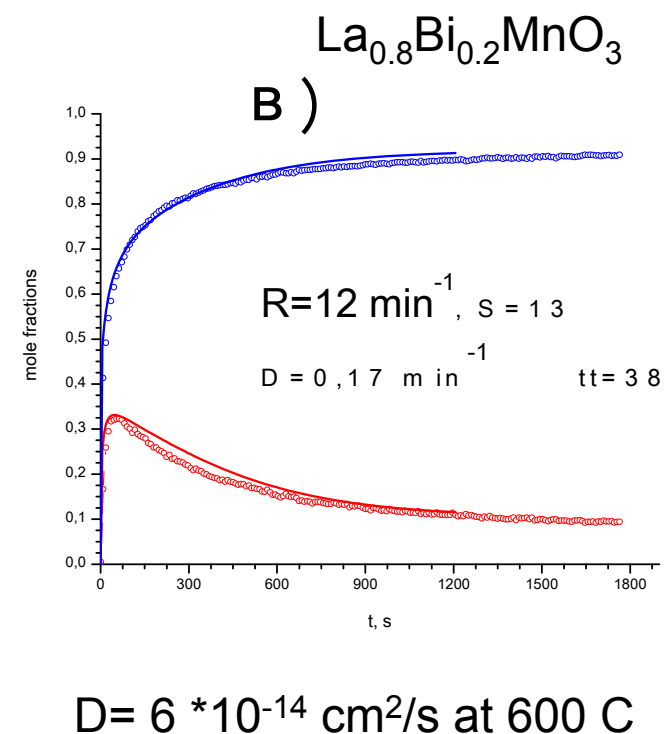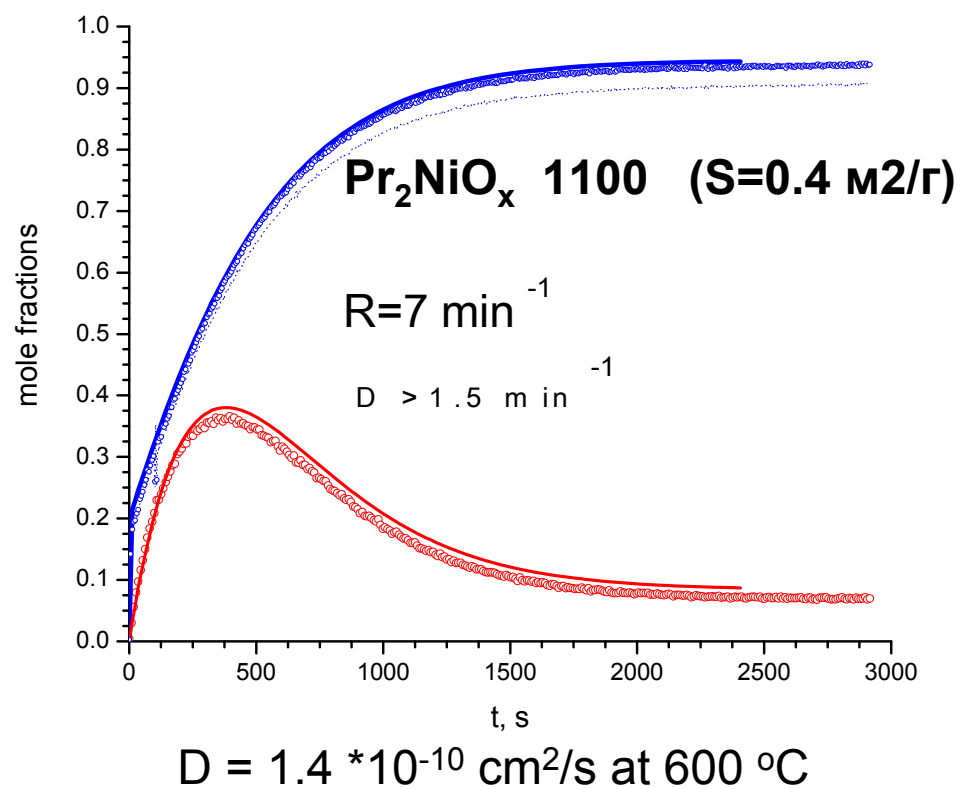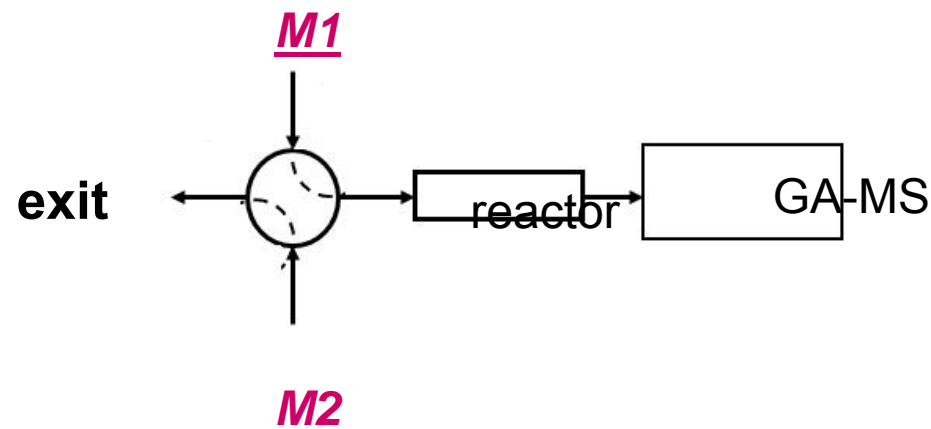
SSITKA set of equations

$$c_{O_2}\left(\frac{\partial \alpha_g}{\partial t} + \frac{1}{\tau}\frac{\partial \alpha_g}{\partial \xi}\right) = -b\left(0.5R^1 + R^2\right)\left(\alpha_g - \alpha_s\right),$$

$$c_{O_2}\left(\frac{\partial f_{34}}{\partial t} + \frac{1}{\tau}\frac{\partial f_{34}}{\partial \xi}\right) = bR^0\left(2\alpha_g\left(1-\alpha_g\right) - f_{34}\right)$$

$$+ bR^1\left(\alpha_g\left(1-\alpha_s\right) + \alpha_s\left(1-\alpha_g\right) - f_{34}\right)$$

$$+ bR^2\left(2\alpha_s\left(1-\alpha_s\right) - f_{34}\right),$$

$$\frac{\partial \alpha_s}{\partial t} = \left(0.5R^1 + R^2\right)\left(\alpha_g - \alpha_s\right) - \frac{N_{bulk}}{N_S}\frac{D}{h^2}\frac{\partial \alpha_{bulk}}{\partial \eta}\bigg|_{\eta = 0}$$

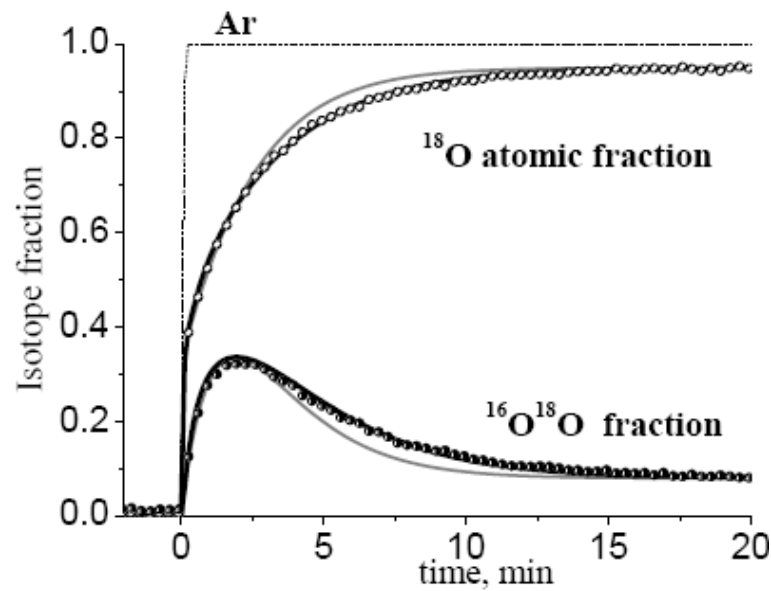$$\frac{\partial \alpha_{Obulk}}{\partial t} = \frac{D}{h^2}\frac{\partial^2 \alpha_{Obulk}}{\partial \eta^2}.$$

The initial and boundary conditions:

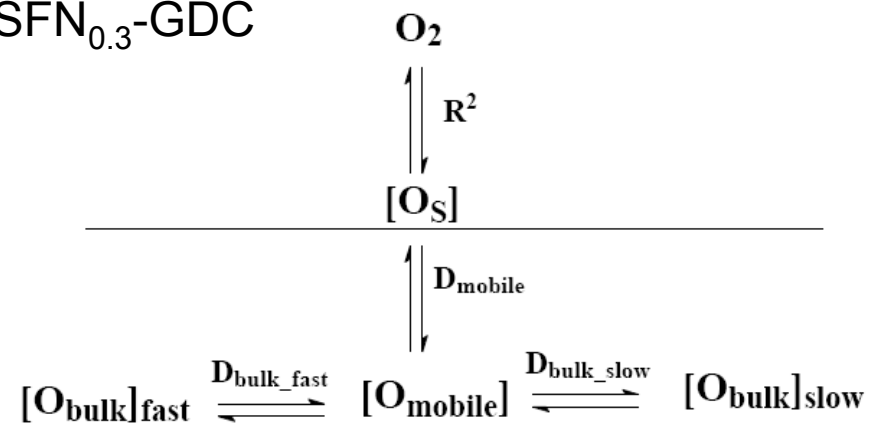$$t = 0: \quad \alpha_g = 0, \quad f_{34} = 0, \quad \alpha_s = 0, \quad \alpha_{bulk} = 0,$$

$$\xi = 0: \quad \alpha_g = \alpha_g^{input}, \quad f_{34} = f_{34}^{input},$$

$$\eta = 0: \quad \alpha_{bulk} = \alpha_s.$$

Oxygen isotope heteroexchange ($^{18}O_2$ SSITKA)

LSFN$_{0.3}$-GDC

Schematic:

O_2
$\updownarrow$ R^2
$[O_S]$
$\updownarrow$ D_{mobile}

$[O_{bulk}]fast \xrightleftharpoons{D_{bulk\_fast}} [O_{mobile}] \xrightleftharpoons{D_{bulk\_slow}} [O_{bulk}]slow$

T, °C	D_F, [cm^2/s]	D_P, [cm^2/s]	$D_{interface}$, [cm^2/s]
Nanocomposite			
600°C	$\geq 6 \times 10^{-14}$	2×10^{-14}	$\geq 1 \times 10^{-8}$
700°C	$\geq 30\times 10^{-14}$	9×10^{-14}	$\geq 5 \times 10^{-8}$
Perovskite			
700		6×10^{-14}	$\geq 0.4 \times 10^{-8}$
Fluorite			
	$>7\times 10^{-14}$		$> 0.2 \times 10^{-8}$

Much faster oxygen diffusion along interfaces